# An infrared study of the L1551 star formation region

Astron. Astrophys. 364, 741–762 (2000)

ASTRONOMY AND ASTROPHYSICS

# An infrared study of the L1551 star formation region

**G.J. White[1,2,11], R. Liseau[1], A.B. Men'shchikov[1], K. Justtanont[1], B. Nisini[6], M. Benedettini[3], E. Caux[12], C. Ceccarelli[4], J.C. Correia[2], T. Giannini[6,3,10], M. Kaufman[5], D. Lorenzetti[6], S. Molinari[7], P. Saraceno[3], H.A. Smith[8], L. Spinoglio[3], and E. Tommasi[9]**

[1] Stockholm Observatory, 133 36 Saltsjöbaden, Sweden
[2] University of London, Queen Mary & Westfield College, Department of Physics, Mile End Road, London E1 4NS, England, UK
[3] Istituto di Fisica Spazio Interplanetario, CNR Area Ricerca Tor Vergata, Via Fosso del Cavaliere, 00133 Roma, Italy
[4] Laboratoire d'Astrophysique de l'Observatoire de Grenoble, 414, Rue de la Piscine, Domaine Universitaire de Grenoble, B.P. 53, 38041 Grenoble Cedex 9, France
[5] San Jose State University, Department of Physics, San Jose, CA 95192-0106, USA
[6] Osservatorio Astronomico di Roma, Via Frascati 33, 00040 Monte Porzio, Italy
[7] California Institute of Technology, IPAC, MS 100-22, Pasadena, California, USA
[8] Harvard-Smithsonian Center for Astrophysics, 60 Garden Street, Cambridge, MA 02138, USA
[9] Italian Space Agency, Via di Villa Patrizi 13, 00161 Roma, Italy
[10] Universita La Sapienza, Istituto Astronomico, Via Lancisi 29, 00161 Roma, Italy
[11] Mullard Radio Astronomy Observatory, The Cavendish Laboratory, Cambridge CB3 0HE, England, UK
[12] CESR, B.P. 4346, 31028 Toulouse Cedex 4, France

Received 29th February 2000 / Accepted 14 August 2000

**Abstract.** Spectroscopic observations using the Infrared Space Observatory are reported towards the two well known infrared sources and young stellar objects L1551 IRS 5 and L1551 NE, and at a number of locations in the molecular outflow. The ISO spectrum contains several weak gas-phase lines of O I, C II, [Fe II] and [Si II], along with solid state absorption lines of CO, $CO_2$, $H_2O$, $CH_4$ and $CH_3OH$. Hubble Space Telescope (HST) images with the NICMOS infrared camera reveal a diffuse conical shaped nebulosity, due to scattered light from the central object, with a jet emanating from L1551 IRS 5. The continuum spectral energy distribution has been modelled using a 2D radiative transfer model, and fitted for a central source luminosity of 45 $L_\odot$, surrounding a dense torus extending to a distance of $\sim 3\times10^4$ AU, which has a total mass of $\sim 13\,M_\odot$. The visual extinction along the outflow is estimated to be $\approx 10$ and the mid-plane optical depth to L1551 IRS 5 to be $\approx 120$.

This model provides a good fit to the ISO spectral data, as well as to the spatial structures visible on archival HST/NICMOS data, mid-IR maps and sub-millimetre radio interferometry, and to ground-based photometry obtained with a range of different aperture sizes. On the basis of the above model, the extinction curve shows that emission at wavelengths shorter than $\sim 2\,\mu$m is due to scattered light from close to L1551 IRS 5, while at wavelengths $\gtrsim 4\,\mu$m, is seen through the full extinguishing column towards the central source. Several [Fe II] lines were detected in the SWS spectrum towards L1551 IRS 5. Although it would seem at first sight that shocks would be the most likely source of excitation for the [Fe II] in a known shocked region such as this, the line intensities do not fit the predictions of simple shock models. An alternative explanation has been examined where the [Fe II] gas is excited in hot ($\sim 4000$ K) and dense ($\gtrsim 10^9$ cm$^{-3}$) material located close to the root of the outflow. The SWS observations did not detect any emission from rotationally excited $H_2$. Observations with United Kingdom Infrared Telescope (UKIRT) of the vibrationally excited $S$- and $Q$-branch lines were however consistent with the gas having an excitation temperature of $\sim 2500$ K. There was no evidence of lower temperature ($\sim 500$ K) $H_2$ gas which might be visible in the rotational lines. Observations with UKIRT of the CO absorption bands close to 2.4 $\mu$m are best fit with gas temperatures $\sim 2500$ K, and a column density $\sim 6\times10^{20}$ cm$^{-2}$. There is strong circumstantial evidence for the presence of dense (coronal and higher densities) and hot gas (at least 2500 K up to perhaps 5000 K) close to the protostar. However there is no obvious physical interpretation fitting all the data which can explain this.

**Key words:** ISM: dust, extinction – ISM: individual objects: L1551 – ISM: jets and outflows – stars: pre-main sequence – infrared: ISM: lines and bands – infrared: stars

*Send offprint requests to*: g.j.white@ukc.ac.uk

## 1. Introduction

Lynds 1551 is one of the most intensively studied molecular outflow sources. Lying at a distance of $\sim 150$ pc in the Taurus-Auriga dark cloud, it is associated with a 30 $L_\odot$ Class I protostar, L1551 IRS 5. This is presumed to be in a pre-T Tauri phase and the driving source of a molecular outflow (Snell et al. 1980; Rainey et al. 1987; Fridlund & White 1989a,b; White et al. 1991), and an optical jet (Mundt & Fried 1983; Fridlund & Liseau 1988). L 1551 IRS5 has long been believed to represent

**Table 1.** ISO observation log. The fluxes of the O I and C II lines are in $\mathrm{Wcm}^{-2}$. All errors and upper limits are $1\,\sigma$

| Name | RA (2000) h m s | Dec (2000) ° ′ ″ | Integration sec | Instrument | O I 63 $\mu$m | O I 145 $\mu$m | C II 157 $\mu$m |
|---|---|---|---|---|---|---|---|
| IRS 5 | 4 31 34.3 | 18 08 05.1 | 4265 | LWS | $1.1\pm0.1\times10^{-18}$ | $\leq 8.5\times10^{-21}$ | $1.5\pm0.3\times10^{-19}$ |
| IRS 5 | 4 31 34.3 | 18 08 05.1 | 6590 | SWS | – | – | – |
| HH 29 | 4 31 28.2 | 18 06 12.7 | 7133 | LWS | $1.5\pm0.1\times10^{-19}$ | $8.6\pm3.1\times10^{-21}$ | $8.3\pm0.6\times10^{-20}$ |
| Flow 3 | 4 30 51.7 | 17 59 00.1 | 7133 | LWS | $5.9\pm1.3\times10^{-20}$ | $7.0\pm4.8\times10^{-21}$ | $7.8\pm0.3\times10^{-20}$ |
| b1 | 4 31 26.3 | 18 07 25.0 | 1937 | LWS | $3.8\pm1.1\times10^{-20}$ | $\leq 4.0\times10^{-21}$ | $9.5\pm0.8\times10^{-20}$ |
| b2 | 4 31 20.5 | 18 07 42.4 | 1777 | LWS | $1.4\pm0.6\times10^{-19}$ | $6.0\pm2.9\times10^{-21}$ | $8.8\pm1.2\times10^{-20}$ |
| b3 | 4 31 16.4 | 18 06 45.1 | 1777 | LWS | $2.4\pm0.8\times10^{-19}$ | $\leq 5.1\times10^{-21}$ | $1.3\pm0.1\times10^{-19}$ |
| b4 | 4 31 12.5 | 18 05 35.8 | 1777 | LWS | $\leq 1.0\times10^{-19}$ | $\leq 5.0\times10^{-21}$ | $7.3\pm0.8\times10^{-20}$ |
| r1 | 4 31 39.8 | 18 07 27.3 | 1937 | LWS | $\leq 1.8\times10^{-20}$ | $\leq 3.1\times10^{-20}$ | $6.7\pm0.9\times10^{-20}$ |
| r2 | 4 31 39.0 | 18 09 57.4 | 1777 | LWS | $1.7\pm0.6\times10^{-20}$ | $\leq 1.2\times10^{-20}$ | $7.6\pm0.8\times10^{-20}$ |
| L1551 NE | 4 31 44.4 | 18 08 32.4 | 1777 | LWS | $4.3\pm0.7\times10^{-19}$ | $\leq 5.4\times10^{-21}$ | $1.4\pm0.2\times10^{-19}$ |
| r4 | 4 31 42.2 | 18 11 24.1 | 1777 | LWS | $\leq 1.0\times10^{-19}$ | $\leq 7.1\times10^{-21}$ | $7.7\pm1.2\times10^{-20}$ |

arche-typically the very early stages of low mass star formation. It is special in that it is closest to the Sun and that it displays its outflow at only a slight inclination angle. In addition, IRS5 is relatively isolated, thus largely reducing source confusion and signal contamination problems, which has made possible observational studies at high resolution and accuracy not obtainable elsewhere. These high resolution studies have revealed that protostars are seemingly far more complex systems than commonly believed. The extinction, $A_{\mathrm{v}}$, towards IRS 5 has been estimated to be $\gtrsim 150^{\mathrm{m}}$ (Smith et al. 1987; Stocke et al. 1988). Continuum maps reveal that the dense central core is surrounded by an extended cloud (Woody et al. 1989; Keene & Masson 1990; Lay et al. 1994). The spectral energy distribution and intensity maps of L1551 IRS 5 have been modelled in detail using radiative transfer methods in spherical (Butner et al. 1991, 1994) and axially-symmetric (Men'shchikov & Henning 1997, hereafter MH97) geometries. These suggest that a flat accretion disc (Butner et al. 1994) or a geometrically thick torus (MH97) lies inside the extended cloud.

High resolution radio observations have shown evidence for a double source located at IRS 5 (Rodríguez et al. 1986, 1999; Campbell et al. 1988; Bieging & Cohen 1985). Other interpretations of the available data suggest a different morphology, with a binary system lying at the centre of IRS 5 whose components are separated by $\sim 50$ AU (Looney et al. 1997), which is in turn surrounded by a dusty disc. Hubble Space Telescope (HST) observations by Fridlund & Liseau (1988) suggest that there are two distinct optical jets, supporting this circumbinary interpretation, and that the central region is surrounded by a torus, with a mass $\sim 0.1$–$0.3\,M_{\odot}$, and a radius of $\sim 700$ AU. This in turn is surrounded by an $\sim 70$ AU central cavity, which contains the double radio source. There appears to be an evacuated cavity in the torus, with a half-opening angle of about 50–55°. The axis of the molecular outflow is inclined at about 30–35° to the line of sight.

In this paper, we report spectroscopic observations obtained with the ISO Long and Short Wavelength spectrometers (LWS, SWS) towards IRS 5, L1551 NE, HH 29 and at a number of locations along the molecular outflow. Archival data from the HST/NICMOS camera and using an infrared spectrometer at UKIRT are also examined to provide constraints to the modelling. We then present a detailed self-consistent two-dimensional continuum radiative transfer model for IRS 5 which is consistent with the available data.

## 2. The observations

In this study, the Infrared Space Observatory (ISO) spectrometers (ISO – Long wavelength Spectrometer – LWS – Clegg et al. 1996, and Short Wavelength Spectrometer – SWS – de Graauw et al. 1996) were used to obtain spectra towards IRS 5 and at 10 positions on the outflow, as summarised in Table 1. Some of these pointing positions lay along the centre of the outflow axis, and some at the edge of the outflow cavity (see Fig. 1).

An ISO SWS spectrum was obtained towards IRS 5 using the S01 mode (2.4–45 $\mu$m, scan speed 4, resolution $\sim$ 1000–2000, integration time 6590 seconds). The SWS aperture varied from $14''\times20''$ to $17''\times40''$ for the 2–40 $\mu$m regions respectively (de Graauw et al. 1996). The SWS and LWS data were reduced using the standard ISO analysis software ISAP v1.6 and LIA 6. Small corrections were made for fringing, and to align adjacent detector scans, but overall the standard pipeline data was of high quality. The SWS observations were made with the long dimension of the slit oriented at position angle 171° (measured anticlockwise from north) – this lies almost orthogonal to the direction of the outflow jet (see Fig. 2) and limb-brightened outflow lobes (Rainey et al. 1987).

Images were taken from the HST archive to examine the near-infrared distribution closer to IRS 5. These data, using the HST/NICMOS camera were cleaned of residual cosmic rays which remained after the standard pipeline processing and mosaicked together. Narrow band images of the $\lambda$ 2.12 $H_2$, $\lambda$ 1.87 Paschen lines were examined, as well as broad filters which included the $\lambda$ 2.12 $H_2$ + CO band-head region, the $\lambda$ 1.64 [Fe II] line, and a 1.12 $\mu$m continuum filter (in this paper we will adopt

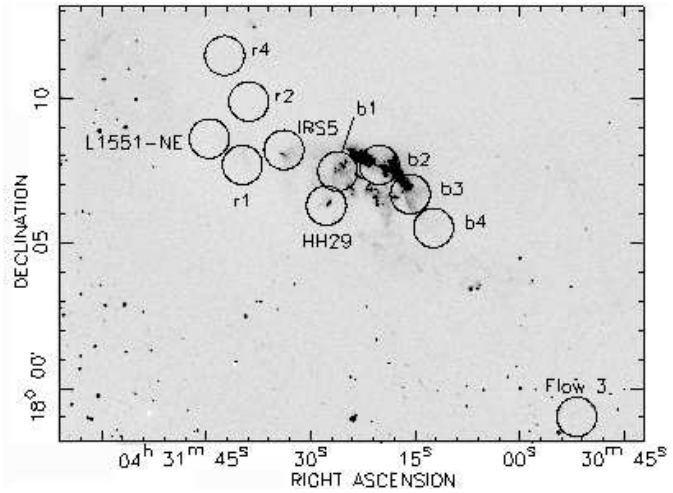


**Fig. 1.** Palomar POSS II Digital Sky Survey picture of the L1551 region, with the position and names of the LWS pointing positions indicated, along with the beamsize, which was $\sim 80''$ (Clegg et al. 1996; Swinyard et al. 1996).

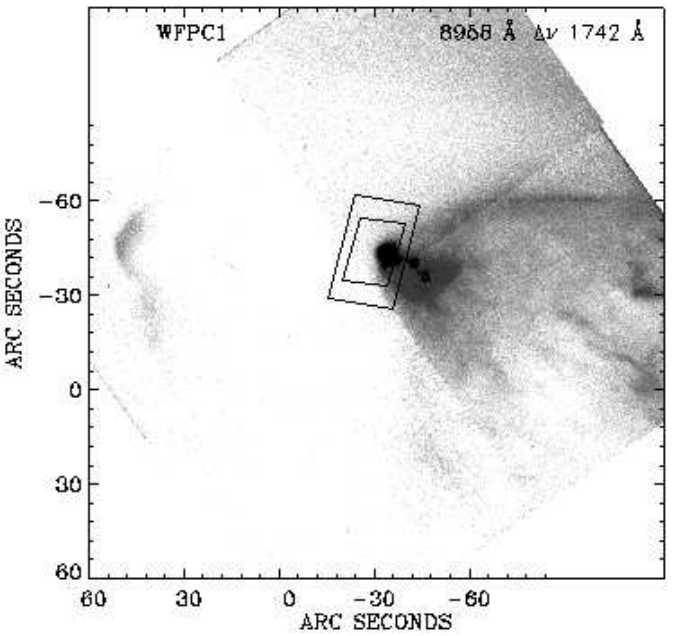


**Fig. 2.** HST image of the central part of the reflection nebula close to L1551 IRS 5 centred at 8900 Å. The SWS apertures at the shortest and longest wavelengths are shown as boxes centred at the co-ordinates listed in Table 1. The two knots visible to the right of the larger SWS aperture are features known from previous optical studies to be associated with working surface or shock activity (Fridlund & Liseau 1988).

a naming convention for lines of the form $\lambda\,2.12$ $H_2$, to mean the $H_2$ line at 2.12 $\mu$m).

Near-infrared long-slit grating spectroscopy was available from the UKIRT CGS4 archive. The CGS4 camera contained a $256 \times 256$ InSb array, and was operated as a long-slit spectrograph covering the 1–5 $\mu$m spectral region. A 75 l/mm grating provided a resolving powers of $\sim$ 500 along an $80''$ slit, which was $1\farcs22$ wide. Spectra covering the interval 1.86 to 2.52 $\mu$m were reduced using the standard STARLINK package CGS4DR, and calibrated against the standard stars BS 1001 and BS 1665.

## 3. Infrared continuum

### *3.1. ISO observations*

#### 3.1.1. SWS and LWS continuum

The ISO spectrum of L1551 IRS 5 is shown in Fig. 3. The shape of the continuum in the LWS spectral region can to first order be fitted by a 50 K blackbody. There is however no reason to believe that the entire central region can be described by blackbody emission at this single mean temperature. In fact, the emission at short wavelengths exceeds the expected blackbody values, indicating that higher temperature dust grains must be present, and that the absorption efficiency of dust grains falls off with wavelengths (see e.g., Fig. 9).

There is a discontinuity in the continuum flux level between 40 and 50$\mu$m – where the SWS and LWS spectra join together (see Fig. 9 for the error bars). This may be due either to a calibration mismatch between the SWS and LWS spectrometers, or a consequence of the different beamwidths.

It is known that the size of L1551 IRS 5 at 50 $\mu$m is less than $6''$ FWHM (Butner et al. 1991), and so it should appear point-like to both the SWS and LWS. One should keep in mind, however, the fact that the beam size of the KAO observations was $14''$, much smaller than the apertures used in this study. Since larger beams probe different volumes of the circumstellar envelope, the observations cannot be compared directly, unless a detailed radiative transfer model for the object is developed. In fact, our detailed model of L1551 IRS 5 presented later in this section, shows that this continuum level break could be entirely due to the difference in beam sizes for SWS and LWS spectrometers – although of course there is still systematic uncertainty between the calibrations of the LWS and SWS as discussed earlier.

#### 3.1.2. Solid state features

The ISO spectra are shown in Fig. 4 and 5. These include a number of features which are attributable to solid state carriers, as well as several gas phase lines.

The spectral region from 2.8 to 3.8 $\mu$m has a broad absorption feature extending across it, made up from contributions from ices at $\sim$ 3.1 $\mu$m, O–H stretching band of $H_2O$ from 3 to 3.4 $\mu$m, and solid $CH_3OH$ at 3.54, 3.84 and 3.94 $\mu$m (Dartois et al. 1999), which sits on the long wavelength side of the $H_2O$ line.

The column density, $N$, of an absorbing species producing a feature of peak optical depth $\tau_{\max}$ and width $\delta\nu$ is given by

$$N = \frac{\tau_{\max}\,\delta\nu}{A} \qquad (1)$$

where $A$ is the integrated absorption cross section per molecule (also known as the band strength) and $\delta\nu$ is the full-width at

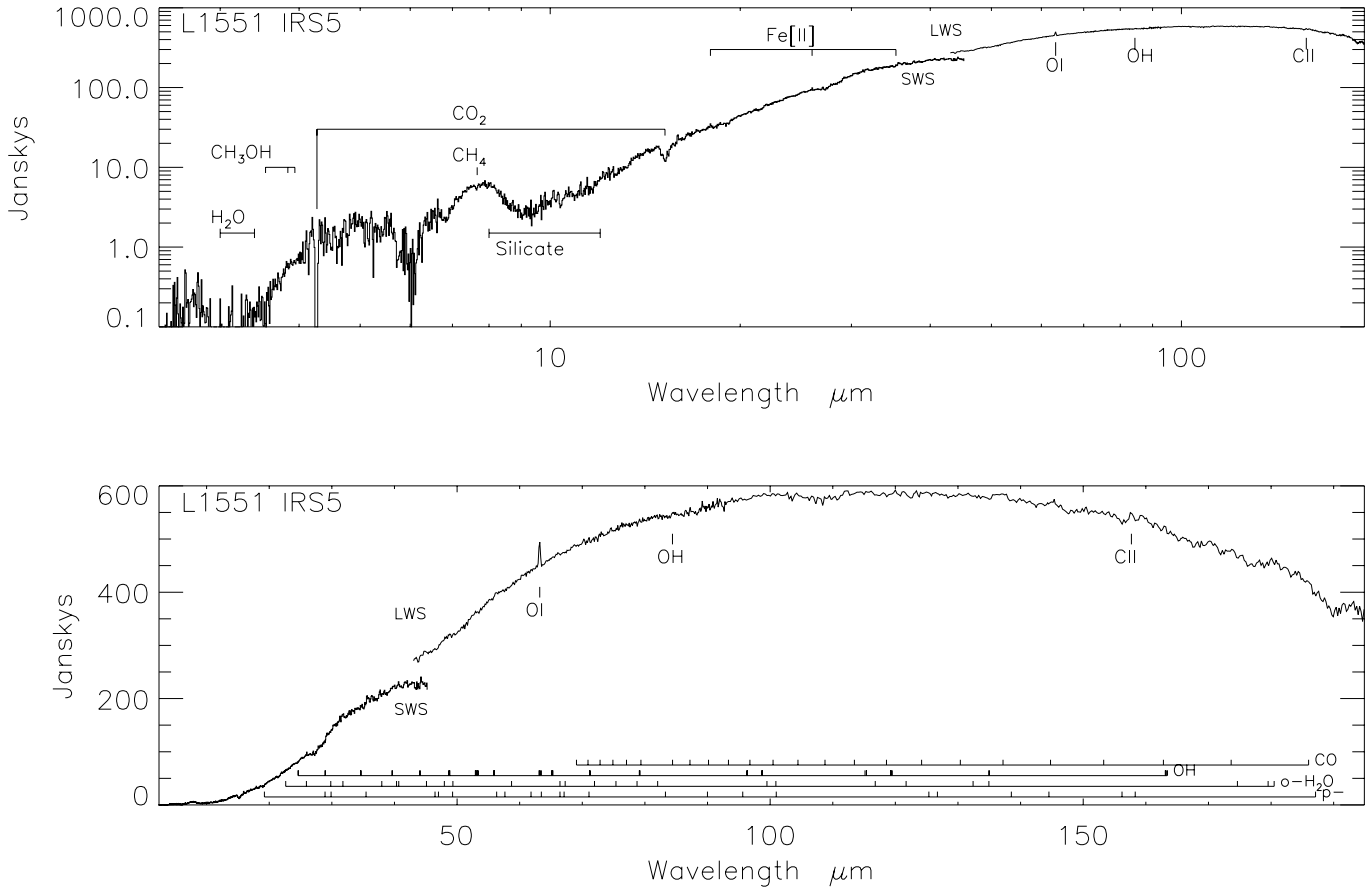


**Fig. 3.** L1551 IRS 5 spectrum. The two graphs show the same data, but using either linear or log scales, so as to emphasise the dynamic range of the spectrum, whilst showing weak features. The upper figure is overplotted with the positions of detected lines in the LWS range, and the locations of various features in the SWS range discussed in the text. The lower figure is overplotted with the locations of molecular emission lines which have been detected by ISO towards other sources.

half maximum intensity, expressed in units of wavenumbers. The lower limit to the column density of solid $H_2O$ is $7.7\times10^{18}$ cm$^{-2}$ (the lower limit is a consequence of the available signal-to-noise ratio (S/N), baseline uncertainty and blending with the nearby $CH_3OH$ emission). Examples showing the optical depth in other solid state features are presented in Fig. 5.

It proved difficult to unambiguously separate the contributions of $CH_3OH$ from the O–H stretching band of $H_2O$, however from first order Gaussian fitting, we estimate the solid $CH_3OH$ column density is $2.6\times10^{18}$ cm$^{-2}$.

The $CO_2$ $\lambda\,4.27$ stretching mode and $CO_2$ $\lambda\,15.2$ bending mode lines are clearly seen in absorption with optical depths $\sim$ 2 and 1 respectively. The $CO_2$ $\lambda\,15.2$ line has an integrated line flux of $-3.72\pm0.5\times10^{-18}$ W cm$^2$ and an optical depth of 0.4. Taking values of band strengths from Gerakines et al. (1995), the column densities in these $CO_2$ stretching and bending modes are $5.5\times10^{17}$ cm$^{-2}$ and $5.3\times10^{17}$ cm$^{-2}$ respectively.

The 'XCN' $\lambda\,4.619$ line reported by Tegler et al. (1993) was not seen in our data, despite detection of the nearby $CO_2$ $\lambda\,4.38$ line. Similarly, the $\lambda\,4.68$ line detected by Pendelton et al. (1999) was also not convincingly present towards L1551 IRS 5.

An absorption feature is seen close to 6 $\mu$m (see also Fig. 5), which is probably due to a combination of water ice, HCOOH and PAH features. Absorption at these wavelengths has previously been proposed by Tielens et al. (1984) and identified by Keane et al. (1999) towards several sources, and seen towards several of the infrared sources towards the Galactic Centre by Chiar et al. (2000), where it is suggested to indicate the presence of a mixture of $H_2O$, $NH_3$, HCOOH and an aromatic C–C component.

An absorption feature associated with the 7.66 $\mu$m $CH_4$ $\nu_4$ 'deformation mode' line is clearly visible, with an optical depth $\tau$ = 0.07. Using a band strength of $A = 7.3\times10^{-18}$ cm molecule$^{-1}$ (Boogert et al. 1996), we estimate the column density of solid methane to be $7.6\times10^{16}$ cm$^{-2}$. Boogert et al. (1996) suggest that the $CH_4$ is embedded with a mixture of polar molecules (such as $H_2O$, $CH_3OH$, $CH_4$ or other species) in the icy grain mantle. However, despite the availability of models of $CH_4$ in various mixtures of polar molecules, the S/N of the present data is insufficient to discriminate between various mixtures.

The column densities estimated above for the various solid state features are summarised in Table 2.

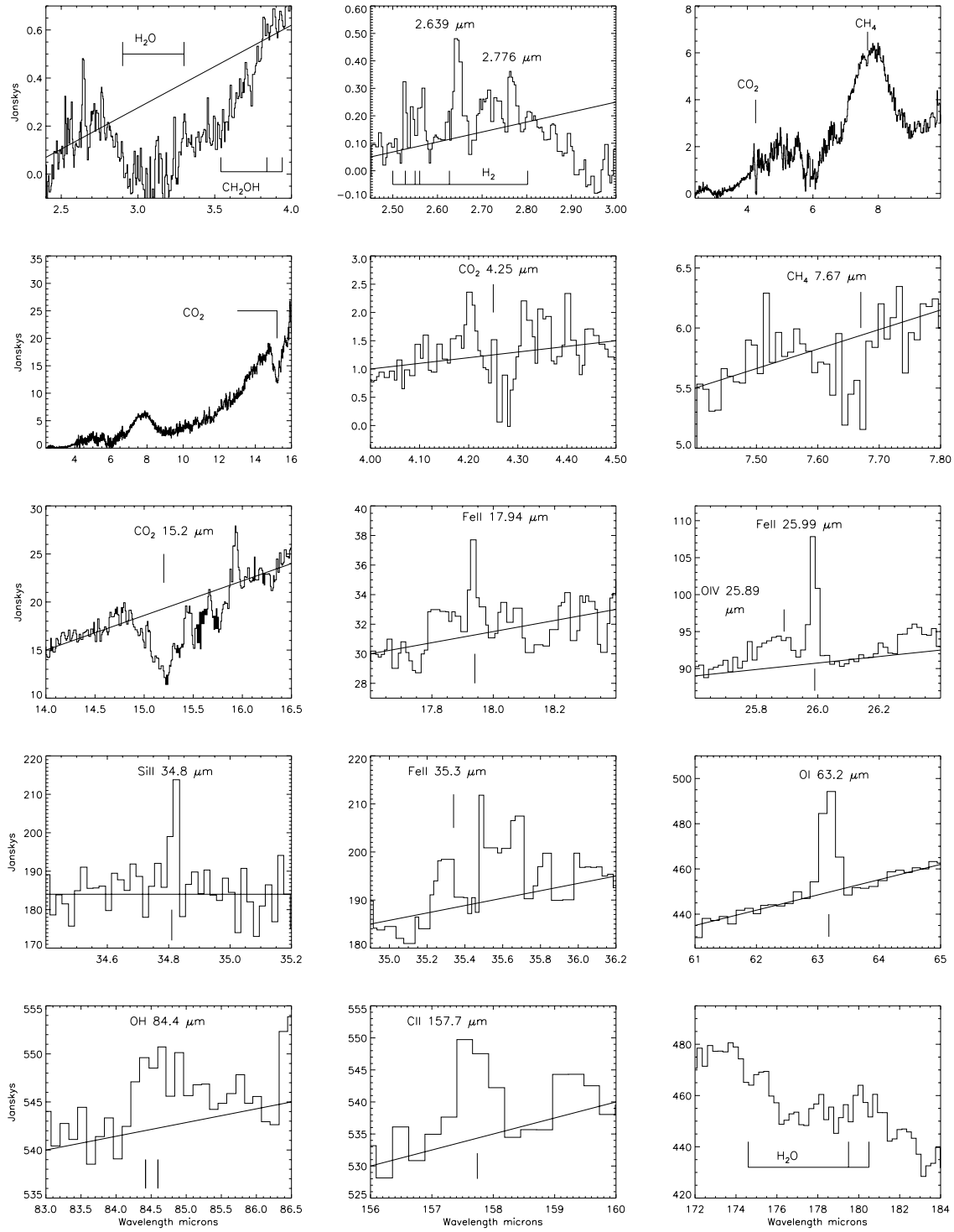


**Fig. 4.** Lines detected in the L1551 IRS 5 spectrum. The $H_2O$ lines indicated in the lower right pane show the expected wavelengths, but do not to necessarily indicate detections.

### 3.1.3. Spectral shape

Compared to many pre-main sequence objects with outflows which have been observed with the ISO LWS, it is striking how few lines have been detected in these very deep spectra (Saraceno et al. 1999). The low intensity of the C II line and the relative invariance of its strength with distance from IRS 5 shows that the UV field must be weak, even close to IRS 5 and the HH 29 region. The non-detection of high-$J$ CO lines suggests that the outflow gas is neither very hot ($T_{\rm ex} \leq 200$ K), nor very dense ($n_{\rm H_2} \leq 10^4$ cm$^{-3}$).

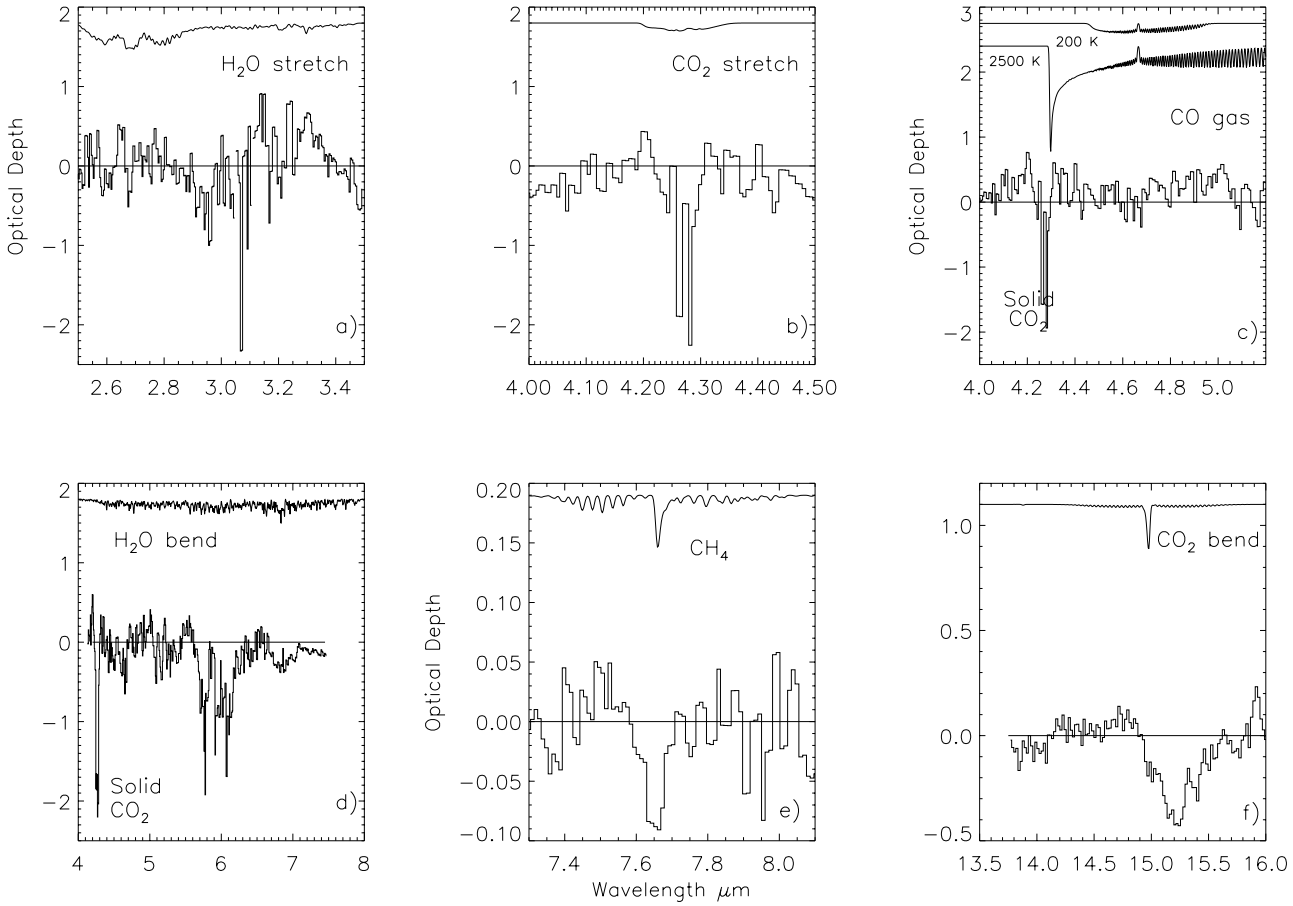


**Fig. 5a–f.** Optical depth in various lines, superimposed by model fits to various gas phase lines. These models are run for a gas temperature of 200 K and Doppler width $\nu_{\rm D} = 2$ km s$^{-1}$, and column densities of **a** $10^{21}$ cm$^{-2}$, **b** $5\times10^{19}$ cm$^{-2}$, **c** $6\times10^{20}$ cm$^{-2}$ (uppermost model curve at the top of the figure was run for a temperature of 200K, the lower model curve was for the higher temperature of 2500 K, and shows the bandhead more clearly), **d** $10^{21}$ cm$^{-2}$, **e** $7^{16}$ cm$^{-2}$, **f** $5\times10^{19}$ cm$^{-2}$. All data and models have an effective resolution of 700.

**Table 2.** Summary of solid state column densities

| Species | $\lambda$ $\mu$m | Band strength cm mol$^{-1}$ | $N_{\rm col}$ cm$^{-2}$ | $N_X/N_{\rm H_2O}$ |
|---|---|---|---|---|
| $H_2O$ | 3 | $2\times10^{-16}$ | $\geq7.7\times10^{18}$ | 1.0 |
| $CO_2$ | 4.27 | $7.6\times10^{-17}$ | $5.5\times10^{17}$ | 0.07 |
| $CO_2$ | 15.2 | $1.1\times10^{-17}$ | $5.3\times10^{17}$ | 0.07 |
| $CH_4$ | 7.66 | $7.3\times10^{-18}$ | $7.6\times10^{16}$ | 0.01 |
| $CH_3OH$ | 3.54 | $2\times10^{-16}$ | $\geq2.6\times10^{18}$ | 0.3 |

### *3.2. HST NICMOS images*

A composite showing images taken from the HST archive is shown in Fig. 6.

The spatial distribution of radiation (Fig. 6) shows a nebular structure with an opening angle of $\sim 60°$. In two of the filters – the [Fe II] and 1.12 $\mu$m broad filters, emission from the 'jet' is clearly visible – most prominently in the [Fe II] filter (this contains the $\lambda$ 1.64 [Fe II] line). It is notable that three [Fe II] lines are also seen in the ISO SWS spectra (see Sect. 4.1), and that the 'jet' is not detectable in the narrowband $\lambda$ 2.12 $H_2$ filter. To attempt confirm the lack of $H_2$ emission from the jet, a first order continuum subtraction, the $\lambda$ 2.12 $H_2$ + CO broad filter was scaled and subtracted from the narrowband $\lambda$ 2.12 $H_2$ filter. The 'continuum subtracted image' formed in this way showed no evidence of $H_2$ emission from the jet down to a level of 2 % of the peak $\lambda$ 2.12 emission. This may be due to the fact that either there is no detectable $H_2$ emission from the jet, or that the $H_2$ emission is exactly cancelled out by the CO bandhead emission contained in the 2.12 $H_2$ + CO broad filter. Resolution of this will require sensitive echelle spectroscopy which is not yet available. By contrast, [Fe II] emission is clearly visible without any attempt to 'continuum subtract'.

The mass of the torus was estimated to be 0.1–0.3 $M_\odot$, the full opening angle was $\sim$ 100–110°, and the radius 630 AU (Lucas & Roche 1996). A similar bipolar geometry of L1551 IRS 5 has been found also by MH97 in extensive modelling which, among other things, has shown that the actual size and mass of the dusty surroundings of IRS 5 is at least an order of magnitude larger ($\sim 10^4$ AU and $\sim 10\,M_\odot$, respectively). The distribution of near-IR emission has been studied towards this source by Lucas & Roche (1996), who used image sharpening techniques to obtain a deconvolved angular resolution with a FWHM of 0.″3.

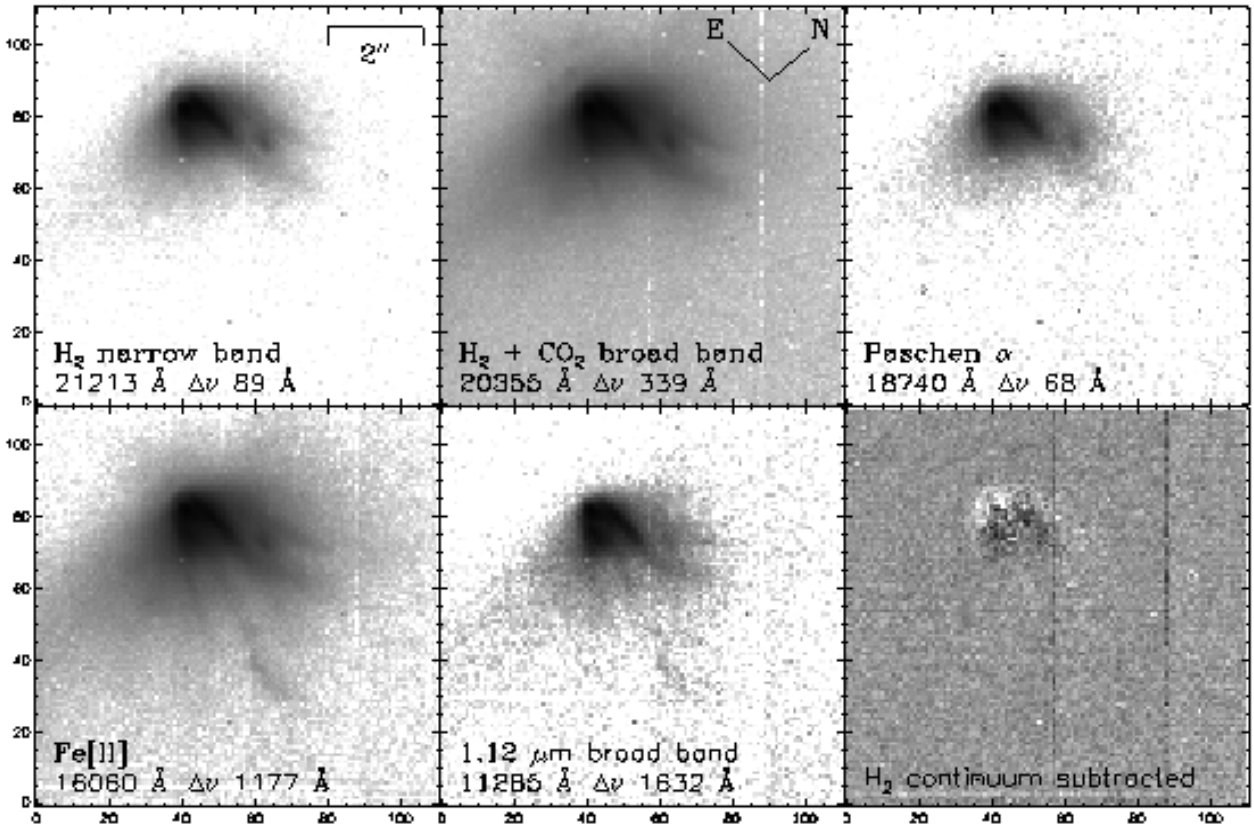


**Fig. 6.** HST images of IRS 5 obtained with the NICMOS 2 camera (total field of view 19.″2 × 19.″2, pixel size 0.″075). The area shown here has dimensions of 8.″2 × 8.″2, and the diffraction limited resolution is ∼ 0.″18. The peak intensity on the continuum subtracted images is 2 % of the peak flux of the direct 2.12 $\mu$m image.

Based on Monte Carlo modelling, they suggested that the light originated from the scattered light associated with a circumstellar torus with an evacuated bipolar cavity.

### *3.3. Two-dimensional radiative transfer model*

In order to interpret the observations in a quantitative way, we constructed a self-consistent two-dimensional (2D) radiative transfer model for L1551 IRS 5. Whereas MH97 have already presented a comprehensive model for this object, their calculations were affected by numerical energy conservation problems resulting from very high optical depths of the model and incomplete convergence of the iterations. The problem, which mainly affected the total luminosity of the central object and the near- to mid-IR part of the SED in the MH97 model, has now been improved (see, e.g., the model of HL Tau by Men'shchikov et al. 1999, hereafter MHF99).

In this paper, we have recomputed the model using the modified version of the code and the new constraints provided by the ISO and HST observations presented above. Our approach and the model are basically the same as those in MH97 and MHF99. We refer to the papers for more detailed discussion of our approach, computational method, model parameters, and ′error bars′ of the modelling.

#### 3.3.1. Geometry

Following MH97, we assume that the central star (or a binary) is surrounded by a dense core (with a radius of ∼ 100 AU), which is embedded within a much larger non-spherical envelope (outer radius of $\sim 3 \times 10^4$ AU). A conical cavity has been excavated by the bipolar outflow, and has a full opening angle of $90^\circ$. This axially-symmetric geometry is the same for both the core and the surrounding material. The geometry is shown in Fig. 7.

The density distributions inside the torus and in the bipolar cavities are functions of only the radial distance $r$ from the centre, where the source of energy is located. We neglect in this model the putative binary system inside the dense core, because its semi-major axis (∼ 20 AU) would be much smaller than the radius of the core. If the binary does exist, it is unlikely that there is a very large cavity around it, with a radius of ∼ 20 AU. Our modelling has shown that in the presence of such a dust-free cavity, most of the inner dust boundary would have temperatures of only ∼ 150 K, far too low to explain the observed SED of L1551 IRS 5. In fact, the near- and mid-IR fluxes would be (many) orders of magnitude less than the observed ones. Instead of assuming that the entire binary fits into the dust-free cavity, we adopt the view that a substantial amount of gas and dust exists deeper inside the core, as close as ∼ 0.2 AU to the central source(s) of energy (see Sect. 4.1.1 later).

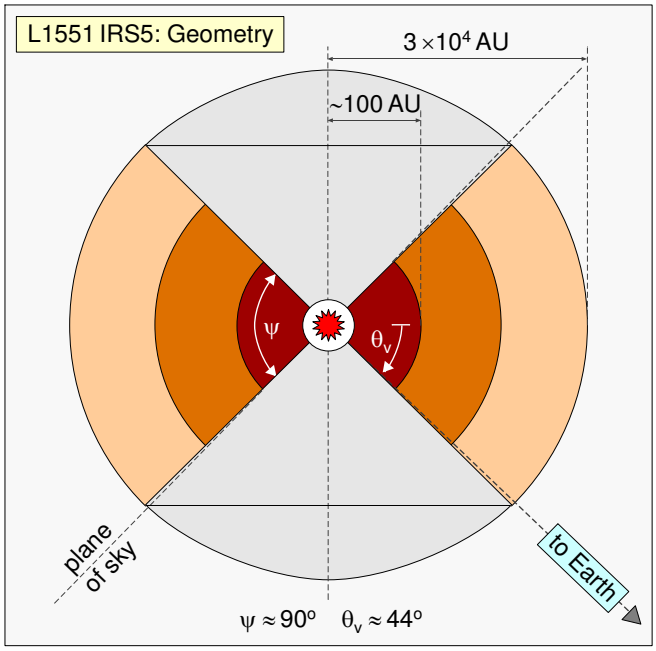


**Fig. 7.** Geometry of L1551 IRS 5. Schematically shown are three regions of the model – the innermost dense torus (dark color), the constant-density part of the envelope (medium color), and the outer extended envelope containing most of the mass (light color). The bipolar geometry is defined by the opening angle of the conical outflow cavities,$\omega = \pi - \psi \approx 90^\circ$ ($\psi \approx 90^\circ$) and the viewing angle, $\theta_v \approx 44^\circ$, between the equatorial plane and the line of sight. The polar outflow regions are less dense than the torus.

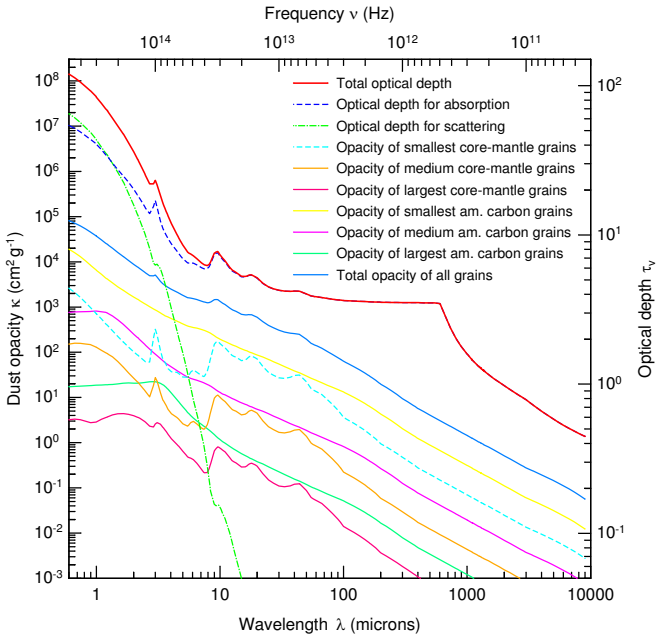


**Fig. 8.** Opacities for our IRS 5 model. Three upper curves show the wavelength distribution of optical depths (total, absorption, and scattering) towards the central source, through both the envelope and the dense torus. The other curves display dust opacities of the core-mantle grains (which exist only in the envelope), for three representative sizes, as well as the total opacity of the entire size distribution.

### 3.3.2. Grain properties

Assuming a similarity between HL Tau and L1551 IRS 5, we adopted for the latter the dust properties proposed by MHF99. The only difference is that magnesium-iron oxide grains ($Mg_{0.6}Fe_{0.4}O$) are absent, because there is no evidence of an emission/absorption sugnature close to 18 $\mu$m that would warrent introdcuing another free parameter to into the model (Fig. 8).

(1) The large dust particles have an unspecified composition, radii 100–6000 $\mu$m, size distribution exponent $p = -4.2$, dust-to-gas mass ratio $\rho_d/\rho = 0.01$, average material bulk density $\rho_{gr} = 2.0$ g cm$^{-3}$, sublimation temperature $T_{sub} \sim 1700$ K. They show a gray (i.e., independent of wavelength) extinction efficiency for $\lambda < 600\,\mu$m, whereas at longer wavelengths it falls off as $\lambda^{-0.5}$.

(2) Core-mantle grains are assumed to contain silicate cores ($Mg_{0.6}Fe_{0.4}SiO_3$) with $\rho_{gr} = 3.2$ g cm$^{-3}$, covered by dirty ice mantles. The ratio of the total core-mantle grain radii to those of the pyroxene cores is 1.4, and their total radii are 0.11–0.7 $\mu$m, $p = -4.2$, $\rho_d/\rho = 0.0037$. The dirty mantles consist of water ice polluted by small amorphous carbon grains. The sublimation temperature of the mantles was assumed to be $\sim 100$ K.

(3) Amorphous carbon grains with radii 0.08–0.5 $\mu$m, $p = -4.2$, $\rho_d/\rho = 0.0063$, $\rho_{gr} = 2.0$ g cm$^{-3}$.

The contibutions to the extinction towards L1551 IRS 5 are shown in Fig. 8.

The first component of very large grains is present only inside the dense torus (0.2 AU$\leq r \leq$250 AU), where all of the smaller grains are assumed to have grown into the large particles. The two other grain components exist only outside (250 AU$\leq r \leq 3 \times 10^4$ AU), in the extended envelope of much lower density. As in any model, the results depend on the accuracy of the input parameters and the assumptions made. A major source of uncertainty in a model such as the one used here, will be the assumptions adopted for the grain properties. Further details on the choice of grain properties and their effect on the model results have been discussed by MHF99 and references therein.

### 3.3.3. Parameter space

As has been discussed in detail by MH97 and MHF99, the parameter space available to numerical modelling is very large. There are many poorly constrained parameters, few of which can be fixed a priori, to reduce the space. This situation requires that all available observational information has to be taken into account to better constrain the models. As in the earlier modelling, we have used as observational constraints all existing photometry data with different beam sizes (from optical to millimetre wavelengths), intensity profiles at 50 $\mu$m, 100 $\mu$m, 1.25 mm, 1.3 mm, and visibility curves from interferometry at 0.87 mm and 2.73 mm (see references in MH97). In addition to the constraints, we used in the new modelling our HST image at 2.12 $\mu$m and the SWS and LWS spectrophotometry presented above.

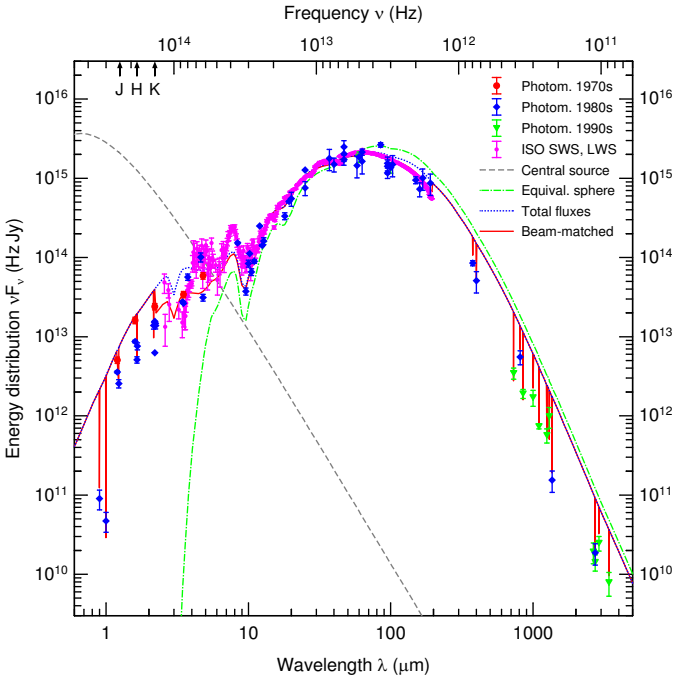


**Fig. 9.** Comparison of the new IRS 5 model with the ISO SWS, LWS spectrum, and various, mostly ground-based, photometric points. The individual fluxes (taken from MH97) are labelled by different symbols, to distinguish between old observations (before 1980, circles), recent ones (1980–1990, diamonds), and new data (after 1990, triangles). Error bars correspond to total uncertainties of the observations. The stellar continuum (which would be observed, if there were no circummstellar dust, is also displayed. The model assumes that we observe the torus at an angle of 44.°5 (relative to its midplane). The effect of beam sizes is shown by the vertical lines and by the difference between the dotted and solid lines in the model SED. Whereas only the lower points of the vertical lines are relevant, we have connected them to the adjacent continuum by straight lines, to better visualise the effect. To illustrate the influence of the bipolar outflow cavities, the SED for the equivalent spherical envelope is also shown.

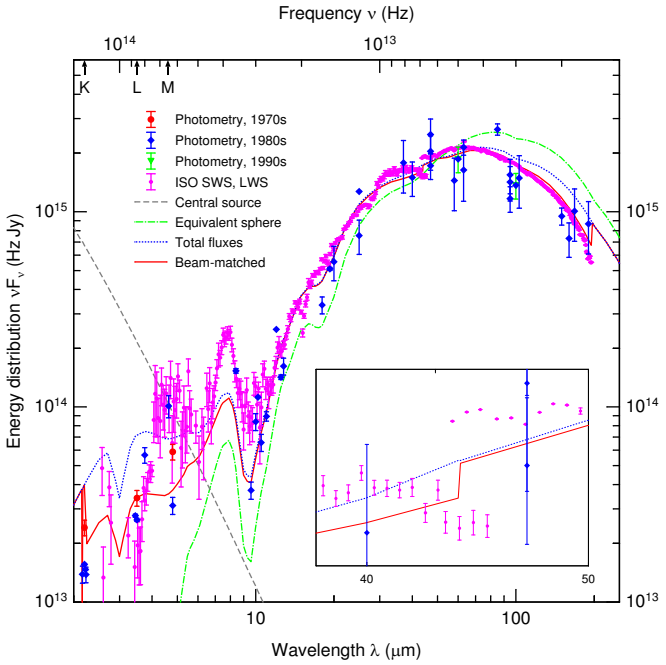


**Fig. 10.** Same as in previous figure but it shows in more detail the SWS and LWS spectrophotometry (2–200 $\mu$m). The small insert displays in even greater detail the region of the ′mismatch′ between the SWS and LWS data (38–50 $\mu$m). The effect of beam sizes is also visible in this plot, as the difference between the dotted and the solid lines in the model SED. To illustrate the influence of the bipolar outflow cavities, the SED for the equivalent spherical envelope is also shown.

**Table 3.** Main input parameters of the IRS 5 model

| Parameter | Value |
|---|---|
| Distance | 160 pc |
| Central source luminosity | 45 $L_\odot$ |
| Stellar effective temperature | 5500 K |
| Flared disc opening angle | 90° |
| Viewing angle | 44.°5 |
| Torus dust melting radius | 0.2 AU |
| Torus outer boundary | $3\times10^4$ AU |
| Torus total mass (gas+dust) | 13 $M_\odot$ |
| Density at melting radius | $8.0\times10^{-13}$ g cm$^{-3}$ |
| Density at outer boundary | $2.6\times10^{-20}$ g cm$^{-3}$ |
| Outflow visual $\tau_v$ | 10 |
| Midplane $\tau_v$ | 120 |

Table 3 lists the *main* input parameters of our model. The opening angle has not been varied, being fixed at the value found by MH97. Likewise, the viewing angle and the outer boundary also have not been varied extensively in our new modelling. We varied mainly the radial density profile and the total mass (or the total optical depth in the mid-plane). The dust grain parameters, the primary source of uncertainties in this kind of modelling, was also mostly fixed at the values adopted by MHF99 for HL Tau.

Numerical parameters related to the accuracy of the model are the number of radial points (277), the number of azimuthal angles for the integration of intensity moments (10), the number of azimuthal angles for the observable flux calculation (50), the number of wavelengths (217), the number of points for convolved intensity maps (600 × 600), and that for the visibility calculations (4000 × 4000). Conservation of the total luminosity for both the equivalent spherical envelope and the 2D model was better than about 7 % at all radial points, certainly good enough compared to the total uncertainties involved in the modelling.

### 3.3.4. Spectral energy distribution

The model SED is compared to the observations of L1551 IRS 5 in Figs. 9 and 10. Only one, best-fitting SED corresponding to the viewing angle of 44.°5 (measured from the mid-plane) is displayed. As has been extensively discussed by MH97 and MHF99 (see, e.g., their Fig. 5), the optical to mid-IR parts of the SEDs of bipolar embedded sources depend strongly on the viewing angle. The viewing angle derived on the basis of 2D radiative transfer calculations depends, among other factors, on the density distribution in the polar direction inside the dense

disc and the surrounding material. Since the real density structure in the vertical direction is generally unknown, we adopted a density distribution independent of the polar angle. This introduces some degree of uncertainty in the derived value of the viewing angle, although the fact that the source is hidden behind the 'wall' of extinction produced by the core and the torus (and close to the apex of the conical cavity) seems to be well established both by observations and by the modelling.

The overall quantitative agreement of the model SED with the entire set of observations of L1551 IRS 5 is obvious. The total model fluxes corrected for the beam sizes (solid lines in Figs. 9 and 10) coincide well with the observed fluxes, except for those in the near IR, although the shape of the SED is still very similar to the observed one. The effect of different apertures is evident everywhere, except for only the mid-IR wavelengths, where the source is very compact and most of its radiation fits into the SWS beam. Note that at millimetre waves the model predicts significantly larger *total* fluxes compared to the observed ones, indicating that the outer envelope is very extended and sufficiently massive.

The insert in Fig. 10 shows that the 'jump' between the SWS and LWS data at $\sim 45$ $\mu$m is a consequence of the different beam sizes. The model shows a clear water ice absorption feature at 3 $\mu$m which is very similar to the observed profile. The agreement of the model with SWS in the 7–9 $\mu$m region is not very good; there are also smaller deviations in the 15–40 $\mu$m part of SWS. As we mostly fixed the grain properties, we have not attempted to find a better fit by varying the dust model (it would be extremely time-consuming). It seems very likely, however, that small changes in the dust chemical composition or temperature profile would be sufficient to fit the SED almost perfectly. We do not believe, however, that such an adjustment makes sense, given the much higher overall uncertainties of the problem at hand.

### 3.3.5. Densities and temperatures

The structure of our model of L1551 IRS 5, which is very similar to that presented by MH97, is illustrated in Fig. 11. The distribution of densities and temperatures in the model were chosen to be similar to those of HL Tau (MHF99), except for the flat density area between 250 and 2000 AU which is very likely to exist in IRS 5. The density structure in the inner few thousand AU is constrained by the SED (Sect. 3.3.4), the submm/mm visibilities (Sect. 3.3.6), and the long-wavelength intensity maps (Sect. 3.3.7). The visibilities suggest that the density structure consists of a dense core inside a lower density envelope. On the other hand, the intensity maps might also imply high densities are present at distances of $\sim 4000$ AU from the central source. Both requirements can however only be reconciled by adopting a flat density distribution. We have no clear understanding of the physical significance of this deduction (also inferred by MH97), which needs to be tested by other observations.

There are three regions that make up the torus: the innermost very dense core with a $\rho \propto r^{-1}$ density gradient, and low-density outer parts with a broken power-law ($\rho = \mathrm{const}$, $\rho \propto r^{-2}$) density profile. A steep $\rho \propto \exp(-r^2)$ transition zone between them (having a half-width at half-maximum of 70 AU) effectively forms the outer boundary of the inner dense torus. The boundary of the torus extends from $\sim 80$ to 250 AU and is effectively truncated by the exponential at about 200 AU, very similar to the density profile of HL Tau (MHF99). Conical surfaces of the bipolar outflow cavities define the opening angle of the torus to be $90^\circ$. Dust evaporation sets the inner boundary at $\approx 0.4$ AU, while the outer boundary is arbitrarily put at a sufficiently large distance of $3 \times 10^4$ AU. The polar outflow cones with a $\rho \propto r^{-2}$ density distribution have much lower density than the torus.

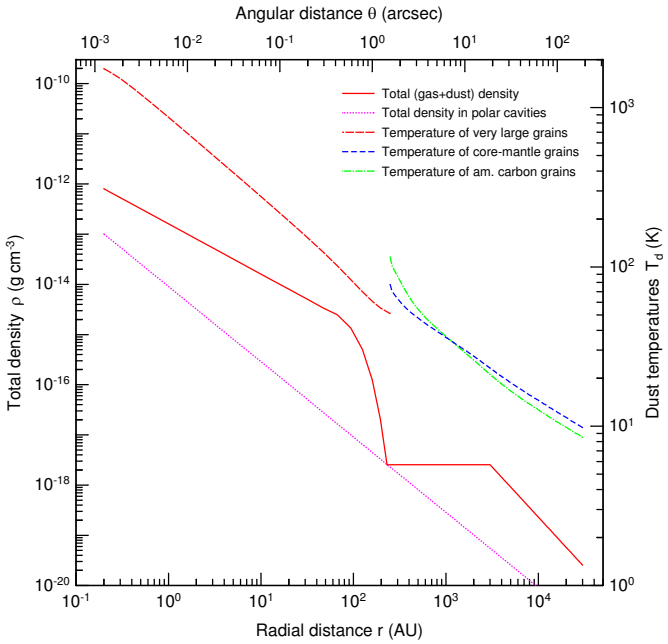


**Fig. 11.** Density and temperature structure of the IRS 5 model. The jump in temperature profiles (upper curves) is due to the difference of grain properties between the dense torus and the outer envelope. See text for more details.

In the absence of any reliable constraints, the conical outflow regions are assumed to have a $\rho \propto r^{-2}$ density profile which is consistent with available data. The temperature profile displays a jump at 250 AU, where the hotter normal-sized dust grains of the envelope are assumed to be coagulated into the large grains of the dense core. We refer to MH97 and MHF99 for a more detailed discussion of the density structure and of the uncertainties of our model.

### 3.3.6. Submillimetre and millimetre visibilities

The model visibilities for two directions in the plane of sky, parallel and orthogonal to the projected axis of the torus (MH97, MHF99) are compared to the available interferometry data in Fig. 12. The model shows good agreement with the spatial information contained in the observed visibilities. The latter do not constrain, however, density distribution in the outer envelope. Instead, intensity maps over a larger area, obtained with large

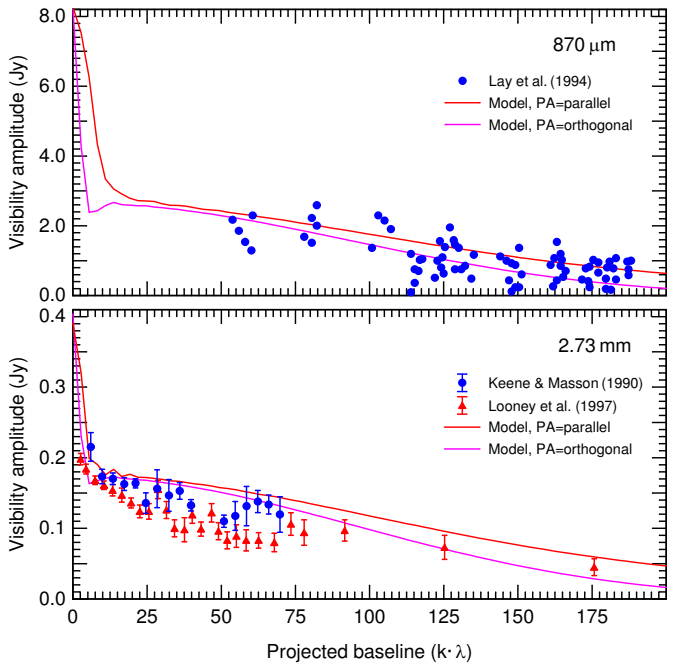


**Fig. 12.** Comparison of the model visibilities at 0.87 mm and 2.7 mm with observations of Lay et al. (1994), Keene & Masson (1990), and Looney et al. (1997). The latter data set was not used in the search through the parameter space of the model (see Sect. 3.3.6). The upper and lower curves show the visibilities for two directions in the plane of sky, parallel and orthogonal to the projected axis of the outflow.

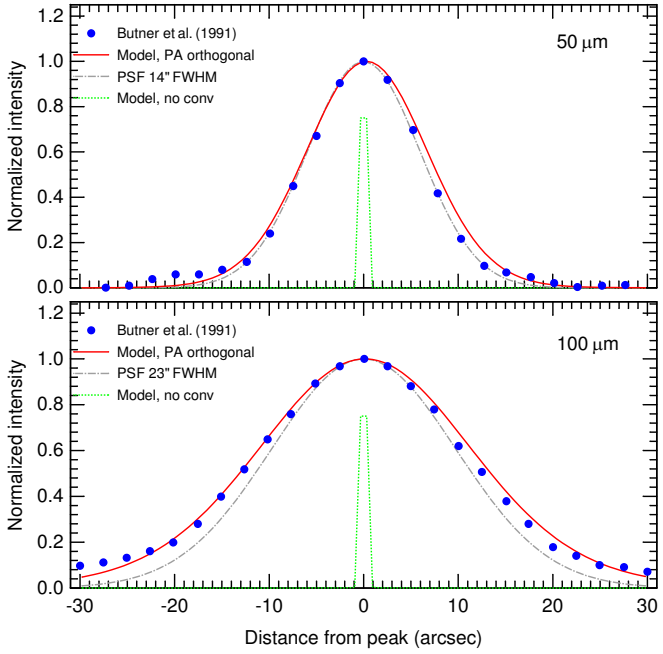


**Fig. 13.** Far-IR intensity profiles for our model of IRS 5 compared to the observations of Butner et al. (1991). Dotted line shows also unconvolved model intensity distribution (normalised to 0.75) that is dominated by the emission of the dense compact torus.

beams, should be useful in determining the density structure on the largest scales, thus giving an idea of the total mass of the circumstellar material. In fact, our model gives much larger mass ($\sim 13\,M_\odot$) and extent ($\sim 3\times10^4$ AU) of the envelope compared to other simplified models which do not take into account all available observations.

The observations by Looney et al. (1997) were added to the figure after our modelling has been completed; they show noticeably lower visibilities compared to those presented by Keene & Masson (1990), which were fit by the model reasonably well. This is clearly a consequence of the assumed $\lambda^{-0.5}$ slope of the opacities by very large grains in this wavelength range (Sect. 3.3.2). The slope has been chosen in our model on the basis of the best fit to both 870 $\mu$m (Lay et al. 1994) and 2.73 mm visibilities (Keene & Masson 1990). The Looney et al. (1997) data suggest that the wavelength dependence of opacity may actually be slightly steeper (closer to $\kappa \propto \lambda^{-0.7}$). This alone or together with a slight modification of the density profile would let the model visibility go through the cloud of the observed points. Given the uncertainties of the different data sets and of our model assumptions, however, we do not feel this would make sense.

### 3.3.7. Far-IR and millimetre intensity profiles

Model intensity profiles at 50 $\mu$m, 100 $\mu$m, 1.25 mm, and 1.3 mm (perpendicular to the outflow direction) are compared with the available observations in Figs. 13 and 14. The model intensity profiles have been convolved with the appropriate circular Gaussian beams. Unconvolved intensity distributions are also shown for reference. As in MH97, the new model shows very good agreement with the measurements, suggesting that the density and temperature distributions of the model are realistic.

Note that the temperature of the outermost parts may be controlled by the external radiation field, which is assumed to be a 5 K blackbody in our model. The radiation field defines the lower limit for the dust temperature in the distant parts of the torus. Thus, it is a key parameter that determines how extended the envelope would appear to millimetre observations after subtraction of the background radiation field. In fact, if the outer radiation field keeps the torus warm (e.g. $\sim 20$ K), then the millimetre intensity maps, which are sensitive to much cooler material, would reveal very little radiation from the envelope. One cannot conclude, however, that an envelope has very little mass on the basis of a few millimetre fluxes alone, without a careful analysis of its density and temperature structure.

### 3.3.8. HST image at 2.12 $\mu$m

An additional check of our model at short wavelengths is enabled by the HST NICMOS image of IRS 5 at 2.12 $\mu$m. In Fig. 15 we compare the model intensity profiles along the same orthogonal directions on the sky, parallel and perpendicular to the axis of the outflow, with the corresponding intensity strips taken from the observed images (Sect. 3.2). The model images were convolved with the HST point-spread function of 0.″18;

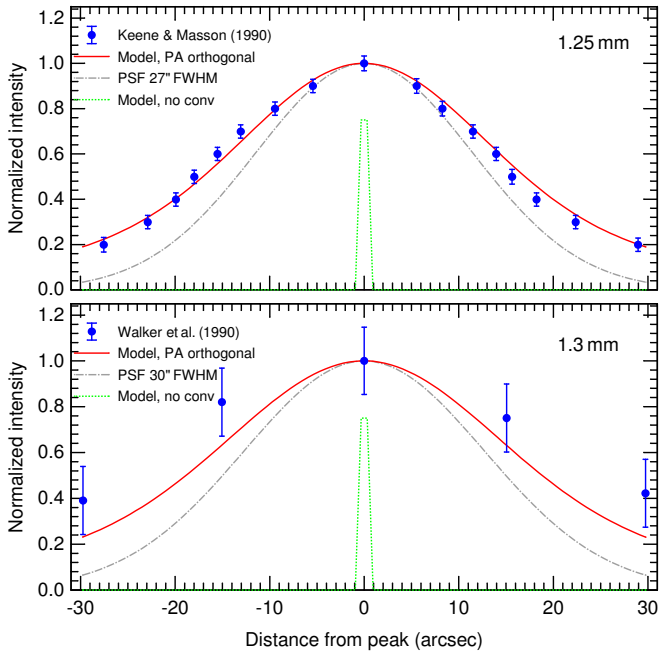


**Fig. 14.** Millimetre intensity profiles of our model of IRS 5 compared to the observations of Keene & Masson (1990) and Walker et al. (1990). Dotted line shows also unconvolved model intensity distribution (normalised to 0.75) that is dominated by the emission of the dense compact torus.

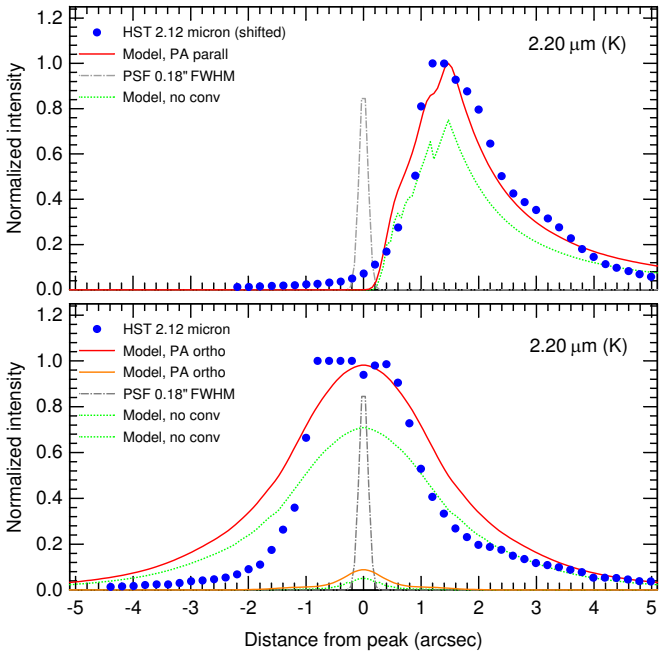


**Fig. 15.** Comparison of the HST 2.12 $\mu$m image with our model of IRS 5 in terms of normalised intensity profiles for two orthogonal directions in the plane of sky. In the top diagram, the $x$-shift of the observed profile is arbitrary, since the absolute positional co-ordinates of the HST are not known to sufficient accuracy – however it is the shape of the distribution that is predicted – and well matched by the model. As in previous figures, we also plotted the unconvolved model intensity distribution (normalised to 0.75) that is dominated by the radiation scattered and emitted by the dense compact torus.

the unconvolved model intensity distributions are also shown for reference. Distortion of the observed profile in the lower panel (plateau and widening of the left wing) is caused by the removal of the intensity spike due to a bright knot slightly off the jet axis on the HST image.

The model of L1551 IRS 5 predicts that the observed intensity peak should be displaced by approximately 1.″5 along the outflow direction from the completely obscured central energy source. This also has been suggested on the basis of the morphology of the optical and radio images (Campbell et al. 1988). Similar displacements in the near-IR images have been found in the recent modelling of HL Tau (see MHF99 for more discussion). Unfortunately the HST/NICMOS images do not have the astrometric accuracy needed to test this idea.

Taking into account the approximations involved in the model geometry and in the radiative transfer method, which should affect our results especially at short wavelengths, the agreement is good. The remaining discrepancies can be explained by a more complex density distribution around IRS 5, which in reality should depend also on the polar angle (MHF99).

In Fig. 16 we have presented near-IR model images of L1551 IRS 5 with a 0.″18 resolution (equivalent to the HST image of the source at 2.12 $\mu$m, Fig. 15). The intensity profiles predicted by our model can be tested by future high-resolution observations.

### 3.3.9. Average density estimates

Table 4 compares average densities of our model with the observational estimates. The density reported by Keene & Masson (1990) (see MH97) from 2.7 mm interferometry was an overestimate because they assumed a steep long-wavelength absorption efficiency of dust grains $\kappa \propto \lambda^{-2}$. Corrected for the higher opacity of large grains adopted in our work, the estimate would be about a factor of 4 times lower, in much better agreement with our result. The model is consistent with observations, given the approximations involved in the problem (see MHF99 for more discussion).

**Table 4.** Average density estimates for L1551 IRS 5 from observations compared to the predictions of our model (references are given in MH97, Table 2).

| Tracer | Rad. $''$ | Rad. AU | Obs. $\langle n_{\mathrm{H_2}} \rangle$ cm$^{-3}$ | Mod. $\langle n_{\mathrm{H_2}} \rangle$ cm$^{-3}$ | Ratio |
|---|---|---|---|---|---|
| $NH_3$ | 60.0 | 9600 | $\approx 1 \times 10^5$ | $1.7 \times 10^5$ | $\approx 1.7$ |
| 1.1 mm | 30.0 | 4800 | $\approx 4 \times 10^5$ | $5.0 \times 10^5$ | $\approx 1.3$ |
| 400 $\mu$m | 17.5 | 2800 | $\gtrsim 1 \times 10^6$ | $8.0 \times 10^5$ | $\lesssim 0.8$ |
| $C^{18}O$ | 13.8 | 2208 | $\gtrsim 4 \times 10^5$ | $8.0 \times 10^5$ | $\lesssim 2.0$ |
| 1.4 mm | 4.0 | 640 | $\approx 1 \times 10^7$ | $3.7 \times 10^6$ | $\approx 0.4$ |
| $C^{18}O$ | 3.5 | 560 | $\gtrsim 3 \times 10^7$ | $5.0 \times 10^6$ | $\lesssim 0.2$ |
| 2 $\mu$m | 3.0 | 480 | $\gtrsim 4 \times 10^6$ | $7.0 \times 10^6$ | $\lesssim 1.8$ |
| 2 $\mu$m | 2.0 | 320 | $\gtrsim 1 \times 10^8$ | $2.4 \times 10^7$ | $\lesssim 0.2$ |
| 2.7 mm | 0.4 | 64 | $\gtrsim 1 \times 10^{11}$ | $1.0 \times 10^9$ | $\lesssim 0.01$ |

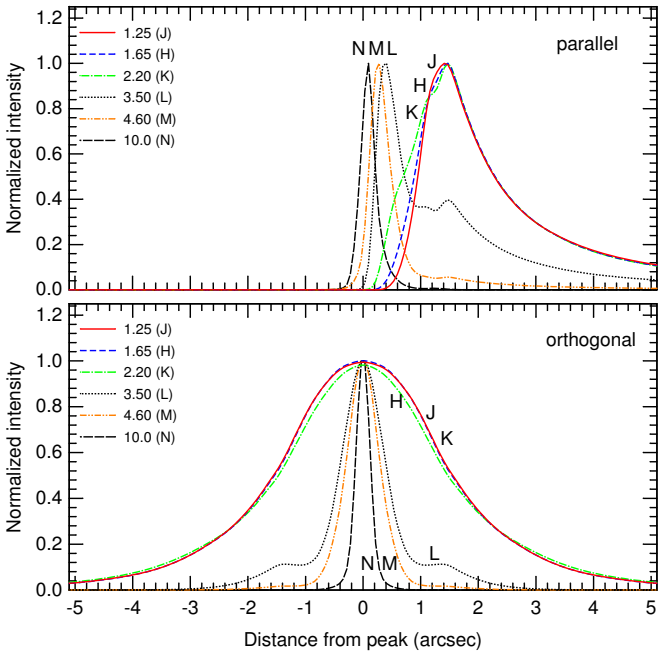


**Fig. 16.** Predictions of our model for $J$, $H$, $K$, $L$, $M$, and $N$ band images of IRS 5 with the adopted point-spread-function of 0.″18 (FWHM). These predictions are included in this paper, because they are now able to be tested using large telescopes such as Gemini with adaptive optics.

## 4. Emission lines

Several narrow emission lines were detected in the L1551 IRS 5 spectrum, specifically [Fe II] $\lambda$ 17.94 and $\lambda$ 25.99, Si II $\lambda$ 31.48, O I $\lambda$ 63.2, OH $\lambda$ 84.4 and C II $\lambda$ 157.7. These can be seen in Fig. 4, and are now discussed by species.

### *4.1. [Fe II]*

[Fe II] line emission is often detected towards starburst galaxies, where it has been interpreted as having been excited by collisional excitation in supernova remnant shocks (Moorwood & Oliva 1988; Lutz et al. 1998). [Fe II] lines have been reported towards several supernova remnants (Oliva et al. 1999a [RCW 103], b [IC 443]), galactic nuclei (Lutz et al. 1996 [SgrA*], 1997 [M82]), and in regions known to have energetic outflows (Wesselius et al. 1998 [S106 IR and Cepheus A]). Optical echelle spectra towards the jet and working surface where the jet interacts with the surrounding medium (Fridlund & Liseau 1988) show linewidths of 100 and 200 km s$^{-1}$ respectively. These results unambiguously show that shock excitation is occurring, although the position of the working surface in L1551 IRS 5 lies outside the SWS field of view. From the raw data, the linewidth of the $\lambda$ 26.0 [Fe II] line, deconvolved from the instrumental resolution, is $\lesssim$ 230 km s$^{-1}$. The ratios [Fe II] $\lambda$ 35.3 / $\lambda$ 26.0 and [Fe II] $\lambda$ 24.5 / $\lambda$ 17.9 should be density sensitive, although their variation over a wide range of densities is only a factor of $\sim$ two. The transitions have high critical densities $n_{\rm cr} \sim 10^6$ cm$^{-3}$ and high excitation temperatures $\gtrsim$ 400 K. As minor coolants, they do not significantly affect the thermal structure of the cloud. To test the possibility that the gas could be photoionised, we ran the photoionisation code CLOUDY (Ferland et al 1998) over a wide range of values. The [Fe II] $\lambda$ 24.5 line is only efficiently excited under conditions of high density ($n_{\rm H_2} \gtrsim 10^6$ cm$^{-3}$) and high UV illumination ($G_{\rm o} \gtrsim 10^6$) (see also Hollenbach et al. 1991) – however, it is impossible to excite the [Fe II] $\lambda$ 17.9 line for reasonable values of ionising flux near L1551 IRS 5, due to the low effective temperature of the star ($T_{\rm eff} \sim 5500$ K). A shocked environment seems a more likely environment to excite the lines. Such a shocked environment could be associated with the optical jet emanating from L1551 IRS 5. We detect emission from [Fe II] $\lambda$ 17.9 and $\lambda$ 26.0 of $9.44 \pm 1.5 \times 10^{-16}$ W m$^{-2}$ and $2.04 \pm 0.3 \times 10^{-15}$ W m$^{-2}$ respectively, with a marginal detection of [Fe II] $\lambda$ 35.3 of $1.62 \pm 0.6 \times 10^{-15}$ W m$^{-2}$. There are further [Fe II] lines at $\lambda$ 5.34, $\lambda$ 51.3 and $\lambda$ 87.4 for which we set 2 $\sigma$ upper limits of $1.05 \times 10^{-15}$, $6.52 \times 10^{-16}$ and $3.6 \times 10^{-16}$ W m$^{-2}$ respectively. The $\lambda$ 5.34 and $\lambda$ 17.9 lines can be used to constrain density, and the $\lambda$ 26 line can be used with other lines as a temperature estimator. However, as pointed out by Greenhouse et al. (1997), Lutz et al. (1998) and Justtanont et al. (1999), other excitation mechanisms such as fluorescence or photoionisation may be important in certain environments.

#### 4.1.1. Observed transitions

A diagram of the lowest energy levels of [Fe II] is shown in Fig. 17 and the major transitions in the range of the ISO spectrometers are listed in Table 5. The observed line fluxes are also given, along with the aperture sizes of the data. From these it is clear that for extended emission several of the line intensity ratios are aperture dependent. Fortunately, some of the potentially most important lines, viz. the 26, 17.9 and 24.5 $\mu$m lines (the 2–1, 7–6 and 8–7 transitions in Fig. 17, respectively), were observed with the same aperture.

The table also lists intrinsic [Fe II] line fluxes, $F_0$, i.e. after a correction for the attenuation by dust extinction has been applied. The values of the dust opacities used for this correction were obtained from the best fit model of the overall SED of IRS 5 (see Sect. 3 and below) and are displayed in Figs. 8 and 18. Contrary to naive expectations, extinction has a considerable effect on the line ratios in IRS 5 even in the mid- to far-infrared. Not only does the temperature diagnostic ratio 17.9/26 become slightly altered, but is actually inverted, changing from the observed value of 0.5 to the ′de-reddened′ one of 2.

Emission lines of [Fe II] detected in the SWS spectrum of L1551 IRS 5 include transitions at 26 and 17.9 $\mu$m. Further, the high excitation lines (cf. Fig. 17) [Fe II] $\lambda$ 1.64 (Sect. 3.2) and $\lambda$ 0.716 (Fridlund & Liseau, in preparation) are also clearly present in this source, as well as the [Si II] $\lambda$ 35 line. Therefore, in the absence of any nearby bright source of UV radiation, excitation of these lines by shocks presents the only known, feasible alternative. However, the comparison of the line intensity ratios for various lines deduced from shock models (Hollenbach & McKee 1989; Hollenbach et al. 1989) with those of the observations makes no immediate sense. In fact, results obtained from

**Table 5.** SWS and LWS aperture sizes at various [Fe II] transitions, observed and dereddened fluxes

| Instrument | Transition | $\lambda$ $\mu$m | $\Omega$ sr | $\Omega/\Omega_{21}$ | $10^{13}\times F_{\rm obs}$ erg cm$^{-2}$ s$^{-1}$ | $(F/F_{21})_{\rm obs}$ | $\tau_{\rm dust}$ | $10^{11}\times F_0$ erg cm$^{-2}$ s$^{-1}$ | $(F/F_{21})_0$ |
|---|---|---|---|---|---|---|---|---|---|
| SWS | 6 – 1 | 5.34 | $6.58\times10^{-9}$ | 0.74 | $< 5.$ | $< 0.25$ | 13.2 | $< 27\,000$ | $< 3\,000$ |
| SWS | 7 – 6 | 17.94 | $8.88\times10^{-9}$ | 1.00 | $9.5 \pm 1.5$ | $0.47 \pm 0.10$ | 5.4 | 21 | 2.4 |
| SWS | 8 – 7 | 24.52 | $8.88\times10^{-9}$ | 1.00 | 3.8 | 0.19 | 4.0 | 2 | 0.2 |
| SWS | 2 – 1 | 25.99 | $8.88\times10^{-9}$ | 1.00 | $20 \pm 3$ | 1.00 | 3.8 | 9 | 1.0 |
| SWS | 3 – 2 | 35.35 | $1.55\times10^{-8}$ | 1.74 | $16 \pm 6$ | $0.80 \pm 0.32$ | 3.5 | 5 | 0.6 |
| LWS | 4 – 3 | 51.28 | $1.81\times10^{-7}$ | 20.4 | $< 3.3$ | $< 0.16$ | 3.1 | $< 0.7$ | $< 0.08$ |
| LWS | 5 – 4 | 87.41 | $1.81\times10^{-7}$ | 20.4 | $< 1.8$ | $< 1.8$ | 2.7 | $< 0.3$ | $< 0.03$ |

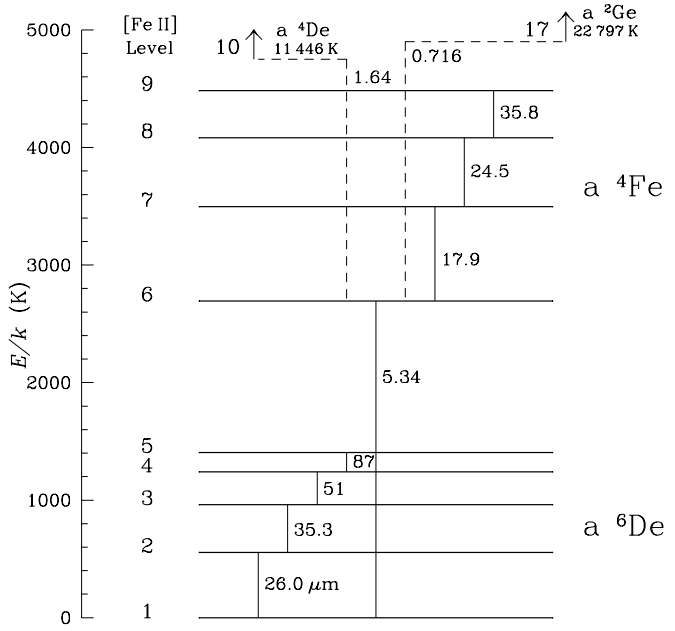


**Fig. 17.** Diagram of the 9 lowest fine structure levels in [Fe II]. The wavelengths of the major SWS and LWS transitions are indicated in $\mu$m next to the solid connecting bars. In addition, two lines from higher states (levels 10 and 17) and which were discussed in the text are indicated by the dashes. Level energies are in the temperature scale (K).

these line ratios (including upper limits to, e.g., the hydrogen recombination lines) lead to diverging conclusions regarding the shock speeds and pre-shock densities in the source. When based on different chemical species, these inconsistencies could possibly be accounted for by differences in the abundances between the source and the models (the models use highly depleted abundances, e.g. for iron $A$ (Fe)= $10^{-6}$, relative to hydrogen nuclei).

At first, an abundance mismatch could also be thought of capable explaining the remarkable strength of the observed mid-infrared emission lines. For instance, the observed flux of the [Fe II] $\lambda$ 26 line, $F_{26,\rm obs} = 2\times10^{-12}$ erg cm$^{-2}$ s$^{-1}$ (Table 5), would imply an intensity of the non-extinguished line $I_{26} > 3\times10^{-2}$ erg cm$^{-2}$ s$^{-1}$ sr$^{-1}$, assuming the jets from IRS 5 to be responsible for the shock excitation ($\Omega_{\rm jets} < 6\times10^{-11}$ sr within the field of view of the SWS; Fridlund et al. 1997). This is, however, significantly larger than the maximum intensity from the published shock models (Hollenbach & McKee 1989, which is $I_{26,\rm mod} = 2\times10^{-2}$ erg cm$^{-2}$ s$^{-1}$ sr$^{-1}$ and which pertains to the extreme parameter values of the models, viz. $n_0 = 10^6$ cm$^{-3}$ and $v_{shock} = 150$ km s$^{-1}$. Therefore, matching the observations would need still higher pre-shock densities ($n_0 > 10^6$ cm$^{-3}$) and would thus be indicative of post-shock densities of the order of $>10^8$ cm$^{-3}$. Such high densities are nowhere observed in or along the jets. The fact that the jet emission in the density sensitive [S II] $\lambda$ 0.6717 to $\lambda$ 0.6734 line ratio is nowhere saturated implies that post-shock jet-densities never exceed a few times $10^3$ cm$^{-3}$ (Fridlund & Liseau 1988). Finally, the dense-and-fast-jet scenario can be ruled out since the expected H I recombination line emission (e.g., Br $\alpha$) that should be excited in this scenario is not observed. In conclusion, it seems obvious that the hypothesis that the lines are excited by one or both of the jets encounters major difficulties.

An alternate model, presented below, provides not only a satisfactory explanation of the observed [Fe II] spectrum, but also a coherent picture of the central regions of the IRS 5 system. An [Fe II] source of dimension a few times $10^{15}$ cm, i.e. twice the size of the central binary orbit ($\sim$ 90 AU), with densities of the order of $10^9$ cm$^{-3}$ and at average gas temperatures of about 4000 K is capable of explaining the observed line fluxes. This putative source of emission is situated at the centre of L1551 IRS 5 and seen through the circumstellar dusty material, which attenuates the radiation both by extinction and by scattering (see Figs. 8 and 18). This configuration presumably constitutes the base of the outflow phenomena from IRS 5. The precise nature of the heating of the gas remains unknown, although one obvious speculation would involve the interaction of the binary with the surrounding accretion disc.

#### 4.1.2. [Fe II] excitation and radiative transfer

The model computations of the [Fe II] spectrum made use of the Sobolev approximation. This seems justified, since (a) velocity resolved observed [Fe II] lines have widths exceeding 200 km s$^{-1}$ (e.g., 0.716 $\mu$m; Fridlund & Liseau, in preparation) and (b) according to the above discussion, high velocity shocks are needed to meet the energy requirements of the observed emission. The energies of the [Fe II] levels, Einstein $A$-values and the wavelengths of the transitions were adopted from Quinet

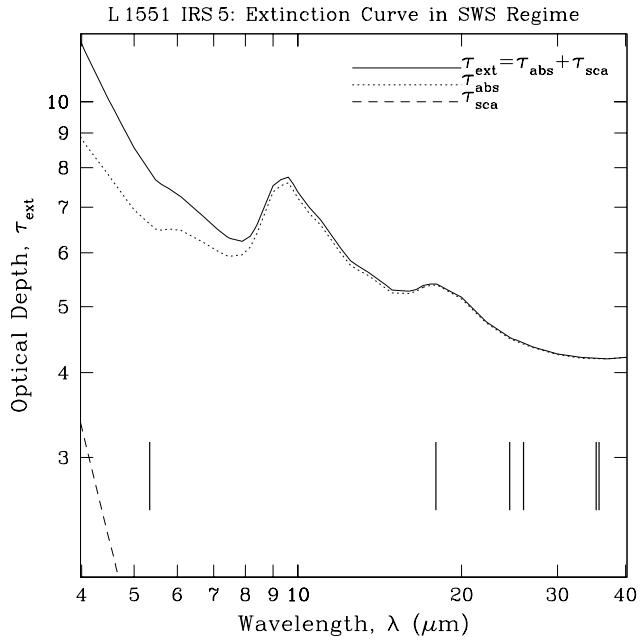


**Fig. 18.** Total dust optical depth towards the centre of IRS 5 (in the SWS wavelength range) according to our 2D radiative transfer model (Sect. 3.3). Also shown are the relative contributions from absorption (dotted line) and scattering (dashed line). The positions of the [Fe II] lines are indicated by the vertical bars. Note specifically the extinction bump, due to silicate particles, at the position of the [Fe II] 17.9 $\mu$m line.

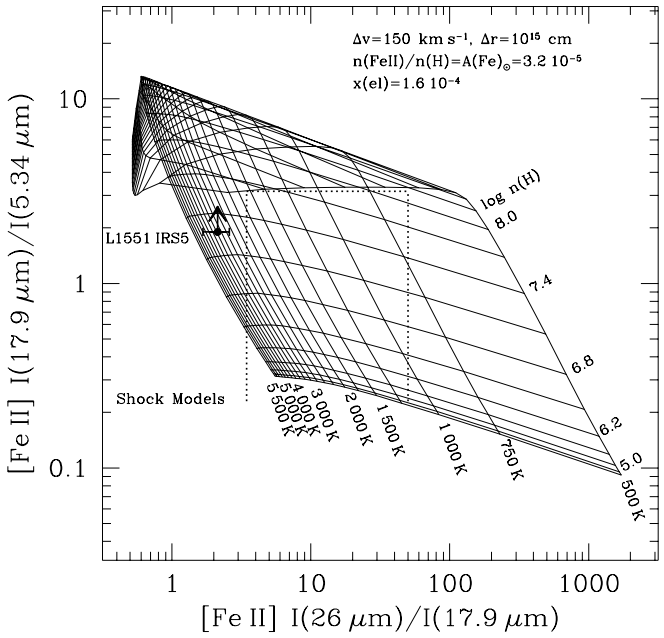


**Fig. 19.** Line ratio diagram for [Fe II] 5.34, 17.9 and 26.0 $\mu$m based on computations discussed in the text. Model parameters are indicated in the upper right corner of the figure. Gas temperatures, $T_{\rm kin}$, run from the right to the left and hydrogen densities, $n$(H), from the bottom to the top, covering a wide range in excitation conditions. The dotted lines identify the area of intensity ratios obtained from planar steady state shock models for shock speeds $v_{\rm s}$=30–150 km s$^{-1}$ by Hollenbach & McKee (1989) and Hollenbach et al. (1989). The arrow-symbol locates L1551 IRS 5 in this diagram, assuming a point source for the SWS observations. We note that the Hollenbach & McKee models are calculated for 1 dimensional, steady state (time independent), non-magnetic and dissociative $J$-shocks. The possible failure of these particular models may not necessarily imply that shock waves are not the main agent of excitation.

et al. (1996). The number of radiative transitions included in the calculation was 1438. These lines are distributed from the FUV to the FIR spectral regions (0.16 to 87 $\mu$m) and the level energies span the range $E/k$ = 0 – 9.1×10$^4$ K (the ionisation potential of [Fe II] corresponds to nearly 1.9×10$^5$ K). The collision rate coefficients were calculated from the work by Zhang & Pradhan (1995), who provide effective collision strengths for 10 011 transitions among 142 fine structure levels in [Fe II]. These are Maxwellian averages for 20 temperatures in the range 1000 K to 10$^5$ K.

No lines of [Fe I] or [Fe III] (or of higher ionisation for that matter) have been detected from IRS 5, so that our assumption that essentially all iron is singly ionised seems reasonably justified. We further assume that iron is undepleted in the gas phase with solar chemical abundance, i.e. $A$(Fe)=3.2×10$^{-5}$ (Grevesse & Sauval 1999). At temperatures significantly below 8000 K the gas would be only partially (hydrogen) ionised. In this case, we assume that the electrons are donated by abundant species with similar and/or lower ionisation potentials. In particular, primarily by Fe and Si plus other metals such as Mg, Al, Na, Ca etc., so that $n_{\rm e} \sim 2.5\,A({\rm Fe})\,n({\rm H})$.

The line intensities were calculated for a range of gas kinetic temperatures and hydrogen densities and an example of the results is presented in Fig. 19. In the figure, intensity ratios for [Fe II] 5.34, 17.9 and 26.0 $\mu$m lines are shown. These lines are connected (see Fig. 17): the 17.9 $\mu$m and 5.34 $\mu$m lines originate from the same multiplet, a $^4$Fe. The upper level of the 17.9 $\mu$m line is at 3500 K above ground and its lower level is the upper level of the 5.34 $\mu$m line, which connects to the ground, and so does the 26 $\mu$m groundstate line (a $^6$De). The corresponding SWS data are also shown in the graph, where the emitting regions have been assumed to be much smaller than any of the apertures used for the observations. These data indicate source temperatures to be somewhere in the range of 3000 to 5000 K and gas densities to be above 3×10$^7$ cm$^{-3}$.

#### 4.1.3. [Fe II] model calculations and results

The model spectrum, ′tuned′ to the SWS observations with the parameters of Sect. 4.1.1, is shown in Fig. 20. The upper panel of the figure displays most of the 1438 lines of the computed intrinsic [Fe II] spectrum, stretching from the far-UV to the far-IR. This spectrum suffers extinction by the circumstellar dust before it reaches the outside observer and is shown in the middle panel. Scattering by the circumstellar dust is of only low significance for the emission in the mid-infrared but is probably important at near-infrared and shorter wavelengths. In the lower panel of Fig. 20, a simple scattering model has been ap-

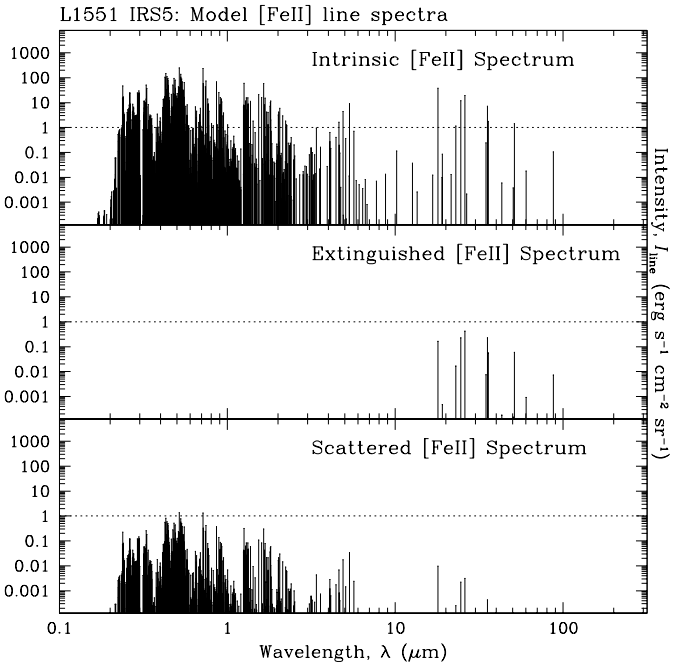


**Fig. 20.** The full [Fe II] spectrum of the discussed computations is displayed, comprising 1438 spectral lines from the far UV to the far IR. **Upper:** The intrinsic emission model of L1551 IRS 5. **Middle:** This spectrum observed through the circumstellar material at IRS 5. **Lower:** The maximum possible amount of scattered [Fe II] line radiation about 1″ off the central source. The dotted horizontal line is meant to aid the eye.

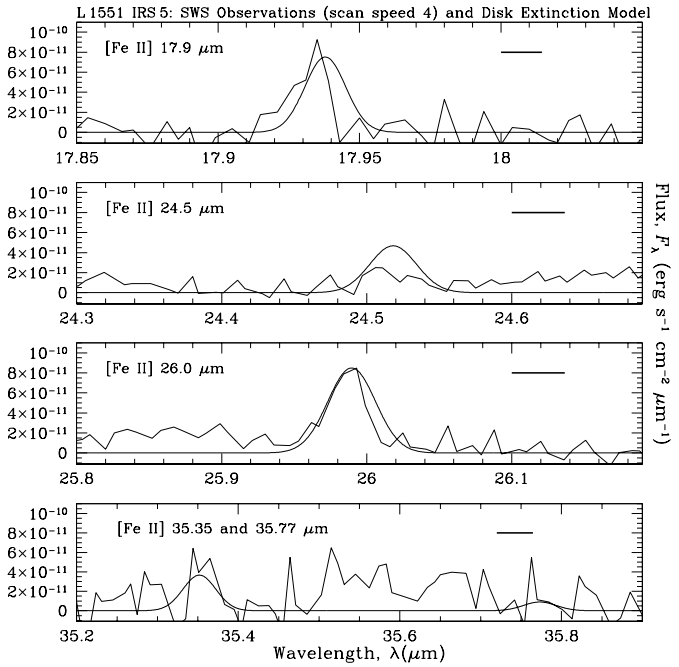


**Fig. 21.** SWS observed spectral segments of four [Fe II] lines (unsmoothed raw data) with a constant local continuum subtracted. Superposed are the model spectral densities, $F_\lambda$ in erg cm$^{-2}$ s$^{-1}$ $\mu$m$^{-1}$, discussed in the text. The source solid angle is $\Omega_{\rm source} = 8.225\times10^{-12}$ sr, corresponding to 90 AU which is of the order of the binary orbit (twice the binary separation). The instrumental function, $R_\lambda$, is that of a point source and scan speed 4 of the SWS; the thick bar indicates the width of a resolution element

**Table 6.** [Fe II] line optical depths and intensities (Model: $T_{\rm kin} = 4000$ K, $n$(H) = $10^9$ cm$^{-3}$, $\log X/({\rm d}v/{\rm d}r) = -10.46$)

| Transition | $\lambda$ $\mu$m | $\tau_{\rm line}$ | $I_{\rm line}$ erg cm$^{-2}$ s$^{-1}$ sr$^{-1}$ |
|---|---|---|---|
| 2–1 | 25.9896 | $2.26\times10^{-2}$ | $1.96\times10^{1}$ |
| 3–2 | 35.3519 | $2.05\times10^{-2}$ | $7.22\times10^{0}$ |
| 4–3 | 51.2847 | $1.20\times10^{-2}$ | $1.42\times10^{0}$ |
| 5–4 | 87.4126 | $4.34\times10^{-3}$ | $1.05\times10^{-1}$ |
| 6–1 | 5.3402 | $1.21\times10^{-4}$ | $9.24\times10^{0}$ |
| 7–6 | 17.9379 | $1.46\times10^{-2}$ | $3.75\times10^{1}$ |
| 8–7 | 24.5182 | $1.15\times10^{-2}$ | $1.20\times10^{1}$ |
| 9–8 | 35.7731 | $5.20\times10^{-3}$ | $1.78\times10^{0}$ |
| 10–6 | 1.6440 | $5.62\times10^{-5}$ | $5.79\times10^{1}$ |
| 17–6 | 0.7157 | $1.58\times10^{-4}$ | $2.36\times10^{2}$ |
| 25–6 | 0.5160 | $3.18\times10^{-4}$ | $2.46\times10^{2}$ |

plied: the displayed spectrum corresponds to the point (about 1″ off the binary centre) where about 1 % of the emitted spectrum is scattered at the efficiencies shown in Fig. 8. The intrinsically strongest transitions (see also Table 6) fall into the visible and near infrared regions of the spectrum and the scattered fraction of this emission may be detectable. Polarimetric line imaging would be helpful in this context, providing valuable insight into the source geometry. This would be of particular relevance to modelling of the $H_2$ line emission (cf. Sect. 4.5), and may help to constrain the grain properties, which would in turn reduce any uncertainty in the computed extinction curve. It is clear that future modelling of this source will need to address a wider parameter space, particularly of grain properties - however this is beyond current computational capabilities.

The spectrum of the adopted model (Table 6) is shown superposed onto selected regions of the observed SWS scans in Fig. 21. The theoretical fit is acceptable for most lines, except perhaps for the 24.52 $\mu$m transition which appears too strong in comparison with the observed line. All of the major [Fe II] lines are thermalised and optically thin, implying that the emission model can be easily scaled by keeping the parameter $N/\Delta v$ constant. For instance, models with higher velocity and lower density (e.g. 300 km s$^{-1}$ and $5\times10^8$ cm$^{-3}$) or vice versa (e.g. 15 km s$^{-1}$ and $10^{10}$ cm$^{-3}$) would still yield the same [Fe II] intensities (but would otherwise disagree with the presence or absence of other lines in the spectrum of IRS 5). The cooling of the gas in all [Fe II] lines amounts to a few times $10^{-3}$ $L_\odot$, which is comparable to the [O I] 63 $\mu$m luminosity, $\gtrsim 7\times10^{-3}$ $L_\odot$. For comparison, the total luminosity generated by the shocks can be estimated as $\max L_{\rm s} = 0.5\, v_{\rm s}^3\, m_{\rm H}\, \mu_{\rm gas}\, n_0 \times {\rm area} \sim 10\, L_\odot$, where we have assumed a gas compression $n/n_0 \sim 10^2$. This amounts to about 20 % of the total radiative luminosity of IRS 5 ($\sim 45\, L_\odot$, Table 3). The largest uncertainty lies in the value of $v_{\rm s}$, the dependence of which is cubic. However, the radiative luminosity of the IRS 5 system can be expected to be dominated by accretion processes, whereas the shock luminosity is prob-

ably generated by mass outflows. To order of magnitude, these estimates would then seem reasonable.

As to how the degree of ionisation of the gas, albeit low, is generated and maintained we have essentially no information. Dissociation, if initially molecular, and subsequent ionisation through shocks seems a likely option. In any case, one would expect the partially ionised gas to produce free-free continuum emission, with a flux density (in mJy) $S_\nu = 5.44\times10^{-13}\,g_{\rm ff}\,(\nu,\,T)Z^2\,T^{-0.5}\,EM\,\exp(-h\,\nu/k\,T)\,\Omega$. From the [Fe II] model, the emission measure of the gas is $EM = \int x_{\rm e}^2\,n^2({\rm H})\,{\rm d}s = 6\times10^6\,{\rm cm}^{-6}\,{\rm pc}$, the free-free Gaunt factor $g_{\rm ff}(1.4\,{\rm GHz},\,4000\,{\rm K}) = 5.0$ and the source solid angle $\Omega = 5\times10^{-12}\,{\rm sr}$. Consequently, we find at 1.4 GHz (21 cm wavelength) $S_{1.4,\,\rm mod} = 3.9\,{\rm mJy}$, which is not far from what has actually been observed. The Very Large Array (VLA) measurements taken in August 1992 by Giovanardi et al. (2000) obtained $S_{1.4,\,\rm obs} = 3.3 \pm 0.3$ mJy are closest in time to the ISO observations.

Recent observations with the SUBARU telescope by Itoh et al. (2000) have shown that the optical jet is dominated by [Fe II] lines, and suggest that the extinction to the jet is on average $A_{\rm v}\sim$ 7 mag. Fridlund et al. (1997) provide observed H $\alpha$ fluxes for the entire jet (ground based and HST), viz. $F({\rm H}\alpha)_{\rm obs} = 4.2\times10^{-14}$ erg s$^{-1}$ cm$^2$ (the working surface, knot D, alone radiates 50 % of this flux; this is not contained inside the observed fields of view of either the ISO-SWS or SUBARU data). Applying the extinction value estimated by Itoh et al. (2000) results in an H $\alpha$ (0.6563 $\mu$m) extinction of $10^{(0.4\times7\times0.79)}\sim165$, so that the intrinsic H$\alpha$ flux of the observed jet would be $F_{H\alpha} = 3.5\times10^{-12}$ erg s$^{-1}$ cm$^2$.

The shock models of Hollenbach & McKee (1989) predict that over the range $v_{shock}$ = 40–150 km s$^{-1}$ and $n_0 = 10^3$–$10^6$ cm$^{-3}$; the intensity ratio of H$\alpha$/[Fe II 26 $\mu$m] should be $\geq$ 30 – 500. Taking the observed value of the 26 $\mu$m line, $F$([Fe II] 26 $\mu$m)$_{\rm obs}$ = $2\times10^{-12}$ erg s$^{-1}$ cm$^2$, would then imply a 'predicted' H$\alpha$ flux F(H$\alpha$)$_0 \geq 6\times10^{-11}$ - $10^{-9}$ erg s$^{-1}$ cm$^2$. This exceeds by more than one order of magnitude, the value inferred for the jet putatively extinguished by 7 magnitudes of visual extinction.

Since the intrinsic line ratio (H$\alpha$/H$\beta$)$_0$ is equal to or larger than 3, dust extinction with $A_{\rm v}$ = 7 mag would result in a line ratio (H$\alpha$/H$\beta$)$_{ext} \geq$ 35 (see, e.g. Appendix B of Fridlund et al. 1993). The observed ratio is (H$\alpha$/H$\beta$)$_{\rm obs}$ = 15 (Cohen & Fuller 1985), which is significantly smaller than the predicted lower limit to the line ratio. This would increase the discrepancy even more.

In summary, it is again concluded that the [Fe II] emission observed by the ISO-SWS is not dominated by the jet, but its source is of different origin. That the jet is emitting in [Fe II] lines has been known for some time and is not new, but the level of emission is not sufficient to explain the SWS observations.

### *4.2. Si II*

The sole [Si II] line detected is the $^2P_{3/2}$ – $^2P_{1/2}$ ground state magnetic dipole transition at $\lambda$ 34.8. It should be one of the major coolants in hot ($T \gtrsim 5000$ K) gas. It has been previously suggested to be a shock tracer (Haas et al. 1986). We detect a flux of $2.35\pm0.3\times10^{-15}\,{\rm W\,m^{-2}}$ from this line. It is of interest to understand to what extent this flux is consistent with the prediction from our model of the central source.

$$F_{\rm line} = \frac{\Omega_{\rm source}}{4\,\pi}\;h\,\nu_{\rm ul}\,A_{\rm ul}\,n_{\rm u}\,\Delta\ell \tag{2}$$

with obvious notations. The fractional population of the upper level, $f_{\rm u}$, is obtained from

$$f_{\rm u} \equiv \frac{n_{\rm u}}{n({\rm Si\,II})} = \left[1 + \frac{A_{\rm ul} + n_{\rm e}\,q_{\rm ul}}{n_{\rm e}\,q_{\rm lu}}\right]^{-1}\,, \tag{3}$$

where the collision rate constants, $q(T_{\rm e})$ (cm$^3$ s$^{-1}$), are related to the respective Maxwellian average of the collision strength, $\gamma(T_{\rm e})$, by

$$q_{\rm ul} = \frac{8.6287\times10^{-6}}{g_{\rm u}\,T_{\rm e}^{1/2}}\,\gamma_{\rm lu} \tag{4}$$

and

$$q_{\rm lu} = \frac{g_{\rm u}}{g_{\rm l}}\,q_{\rm ul}\,\exp-\frac{h\,\nu_{\rm ul}}{k\,T_{\rm e}}\,. \tag{5}$$

At the $2\sigma$ level, upper limits can be set for $F$[Si I] 68.5$\mu$m $< 6.4\times10^{-20}$ W cm$^{-2}$ and $F$[Si III] 38.2$\mu$m$< 3.7\times10^{-19}$ W cm$^{-2}$), whence we can safely assume that essentially all silicon is singly ionised. $n_{\rm u}$ can therefore be expressed as $f_{\rm u}\,A({\rm Si})\,n({\rm H})$, where $A({\rm Si})$ is the abundance of silicon with respect to hydrogren nuclei.

Energy levels and Einstein-$A$ values were adopted from Wiese et al. (1966) and Kaufman & Sugar (1986) and collision strengths from Callaway (1994). As for iron, silicon is assumed to be undepleted in the central core regions of L 1551 IRS 5 and we adopted the solar value of the silicon abundance, $A({\rm Si}) = 3.2\times10^{-5}$ (Asplund 2000).

For the values of the model parameters, viz. $n$(H) = $10^9$ cm$^{-3}$, $n_{\rm e} = 8\times10^4\,{\rm cm^{-3}}$ and $T_{\rm e} = 4\,000\,{\rm K}$, the fractional population becomes $f_{\rm u} = 0.64$. Further, in conjunction with $\Omega_{\rm source} = 8.2\times10^{-12}\,{\rm sr}$ and $\Delta\ell = 90\,{\rm AU}$, the intrinsic model flux then becomes $F_0$([Si II] 35 $\mu$m)$= 2.2\times10^{-10}\,{\rm erg\,cm^{-2}\,s^{-1}}$. Taking the dust extinction by the intervening disk into account, $\tau_{35\,\mu\rm m} = 4.1$ Fig. 18, leads to the predicted estimation of the observable flux, i.e. $F_{\rm model}$([Si II] 35 $\mu$m)$= 3.6\times10^{-12}\,{\rm erg\,cm^{-2}\,s^{-1}}$.

In this undepleted case, the model flux is only slightly larger, by a factor of $\sim$ 1.5, than the actually observed value. We conclude therefore that our model of the central regions in L 1551 IRS 5 is capable of correctly predicting the flux in the [Si II] 35 $\mu$m line. It is likely that most of this emission also originates in these central regions.

### *4.3. OH*

The excitation of OH has been modelled by Melnick et al. (1987), who studied OH emission towards the Orion Nebula.

**Table 7.** Summary of IRS 5 $H_2$ line fluxes

| Line | $\lambda$ | Flux W m$^{-2}$ | | $I_{\rm line}/I_{S(0)}$ | | Thermal | PDR | High $A_{\rm v}$ | | *C*-shock |
|---|---|---|---|---|---|---|---|---|---|---|
| | $\mu$m | 0″ | -1.″2 | 0″ | -1.″2 | 2000 K | | 0″ | -1.″2 | |
| $H_2$ $S(0)$ | 2.223 | $7.9\pm0.8\times10^{-18}$ | $5.6\pm0.1\times10^{-18}$ | 0.72 | 0.93 | 0.21 | | 0.07 | 0.06 | 0.44 |
| $H_2$ $S(1)$ | 2.122 | $1.1\pm0.1\times10^{-17}$ | $6.0\pm0.1\times10^{-18}$ | 1.00 | 1.00 | 1.00 | 1.00 | 1.00 | 1.00 | 1.00 |
| $H_2$ $S(2)$ | 2.034 | $3.9\pm0.4\times10^{-18}$ | $0.5\pm0.1\times10^{-18}$ | 0.36 | 0.1 | 0.37 | 0.28 | 1.13 | 1.59 | 0.23 |
| $H_2$ $S(3)$ | 1.958 | $1.0\pm1.2\times10^{-17}$ | $8.7\pm0.1\times10^{-18}$ | 0.96 | 0.93 | 1.02 | 0.81 | 24.0 | 23.2 | 0.12 |
| $H_2$ $Q(1)$ | 2.407 | $2.0\pm0.1\times10^{-17}$ | $2.3\pm0.8\times10^{-17}$ | 1.84 | 2.67 | 0.7 | 1.58 | 0.01 | 0.01 | 2.43 |
| $H_2$ $Q(2)$ | 2.413 | $5.3\pm0.1\times10^{-18}$ | $7.9\pm0.2\times10^{-18}$ | | 0.49 | 0.23 | 0.37 | | 0.005 | 0.49 |
| $H_2$ $Q(3)$ | 2.424 | $3.1\pm0.1\times10^{-17}$ | $2.7\pm8.0\times10^{-17}$ | | 2.79 | 0.70 | 0.71 | | 0.006 | 0.7 |
| $H_2$ $Q(4)$ | 2.438 | $1.3\pm0.1\times10^{-17}$ | $2.7\pm0.3\times10^{-17}$ | | 1.2 | 0.21 | 0.16 | | 0.002 | 0.07 |
| $H_2$ $Q(5)$ | 2.455 | $1.2\pm0.1\times10^{-17}$ | $5.2\pm0.5\times10^{-18}$ | | 1.11 | 0.59 | | | 0.001 | 0.05 |

Columns 5 and 6 list the observed flux for various transitions relative to the $S(1)$ line, for two positions located a) on source and b) $\sim 1.''2$ southwards along the slit. Columns 7 and 8 contain the line ratios expected, in the absence of any extinction for thermal excitation at 2000 K (Black & van Dishoeck 1987) and for a PDR model taken from Draine & Bertoldi (1996) for $n_{\rm H}\ \sim10^6$ cm$^{-3}$, $\chi = 10^5$ and $T_{\rm o} = 1000$ K. Columns 9 and 10 are the data for the on source and $\sim 1.''2$ southward slit positions, with an extinction correction applied as discussed in Sect. 4.1.1. Column 11 lists values from the $C$-shock modelling of Kaufman & Neufeld (1996) for a 15 km s$^{-1}$ shock propagating in a medium with a pre-shock density $n_{\rm H_2} = 10^{6.5}$ cm$^{-3}$.

The line which at best detected at a low significance level, corresponds to a blend of the $^2\Pi_{3/2}$ $J$= 7/2$^+$ – 5/2$^-$ and $^2\Pi_{1/2}$ $J$= 7/2$^-$ – 5/2$^+$ rotational lines at 84.42 and 84.59 $\mu$m respectively (see Fig. 4). The integrated flux contained in these two blended lines is $1.51\times10^{-19}$ W cm$^{-2}$. Other OH lines within the ISO spectral bands are the $^2\Pi_{1/2}$ $J$ = 9/2 – 7/2 transitions at 55.9 $\mu$m, the $^2\Pi_{3/2}$ $J$ = 5/2 – 3/2 lines at 119.3 $\mu$m and the $^2\Pi_{1/2}$ $J$= 3/2 – 1/2 transitions at 163 $\mu$m, for which we set 3 $\sigma$ upper limits of $3.1\times10^{-20}$ W cm$^{-2}$, $2.9\times10^{-20}$ W cm$^{-2}$ and $5.9\times10^{-20}$ W cm$^{-2}$ respectively.

### *4.4. $H_2O$*

Water emission has already been observed towards a number of molecular outflows with the ISO spectrometers (Liseau et al. 1996; Ceccarelli et al. 1999; Nisini et al. 1999). It is already well understood that the presence or absence of $H_2O$ in a cloud, may be used to trace the shock activity of the gas (Bergin et al. 1998, 1999). We have been unable to identify any $H_2O$ emission from IRS 5 (see Fig. 4), although we set a 2 $\sigma$ upper limit on the 40.69 $\mu$m $4_{32}$–$3_{03}$ line of $3.62\pm1.55\times10^{-15}$ W m$^{-2}$. This is the most intense water line seen in W Hya (Neufeld et al. 1996). No lines were detected towards L1551 IRS 5 at 29.8, 31.8, 174.6, 179.5 and 180.5 $\mu$m, which correspond to strong lines that have been detected from other sources, to upper 2$\sigma$ upper limits of 21, 26, 4, 6 and 6 $10^{-20}$ W cm$^{-2}$ respectively (uncorrected for extinction – see Fig. 18).

### *4.5. $H_2$*

No emission lines were detected from any of the rotational lines of $H_2$ in the SWS spectrum towards IRS 5. A single detection of the $\nu$ = 1–0 vibrationally excited $S(1)$ line at 2.122 $\mu$m has previously been reported by Carr et al. (1987), along with the $Q$-branch lines at 2.407, 2.414 and 2.424 $\mu$m, in a 3.″6 aperture.

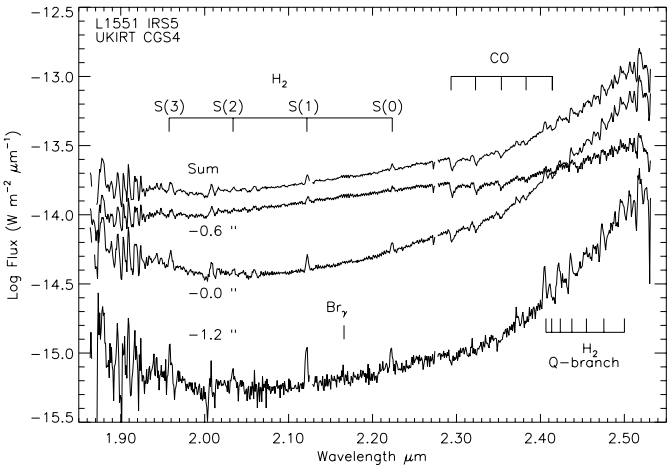


**Fig. 22.** UKIRT archive spectrum towards L1551 IRS 5. This intensity at the (0,0) position is about three times weaker than the Carr et al. spectrum – but in reasonable agreement since the emission is extended relative to the UKIRT beam.

Their reported $S(1)$ flux of $2.8\pm0.3\times10^{-17}$ W m$^{-2}$ lies below the SWS 2 $\sigma$ sensitivity limit at slightly longer wavelengths (the SWS spectrum starts at 2.4 $\mu$m) of $5.6\times10^{-16}$ W m$^{-2}$. In view of the low S/N of the Carr et al. (1987) data, we searched the UKIRT archive for a 2 $\mu$m spectrum to confirm the Carr et al. result. This spectrum is shown in Fig. 22.

The fluxes in the UKIRT observations are summarised in Table 7. From the upper limits to the $\nu$ = 0–0 lines, it is possible to set limits on the beam averaged $H_2$ column densities using an ′excitation diagram′. The extinction corrected intensity of an $H_2$ line $I(\nu'\,J')$ is related to the column density of the line, $N(\nu'\,J')$ by the relationship:

$$I(\nu'\,J') = \frac{hc}{4\pi}\nu A(\nu'\,J')\,N(\nu'\,J') \qquad (6)$$

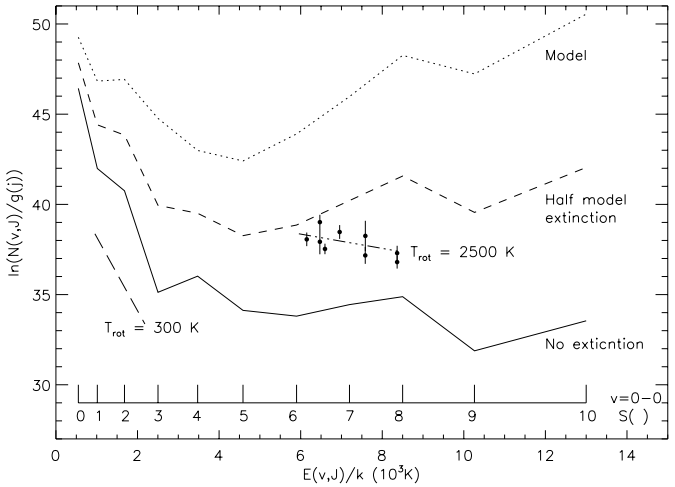


**Fig. 23.** Rotational temperature plot showing the $\nu$ = 0–0 $2\,\sigma$ upper limits (solid, dashed and dotted lines) estimated from the SWS data, and the $\nu$ = 1–0 detections (black circles with $2\,\sigma$ error bars) from the UKIRT data. The SWS upper limits are shown for three cases, with no extinction, with the extinction inferred from our modelling as described in the text, and for illustration, halving the model extinction. We have presented the case that the 2 $\mu$m $H_2$ lines are due to scattered light – thus the column densities estimated from the $H_2$ fluxes given in Table 7 are plotted without any correction for extinction or scattering. A line representing a rotational temperature of 2500 K has been overlaid on the 2 $\mu$m lines, along with $1\,\sigma$ error bars. The $H_2$ column density determined from the vibrationally excited lines is 6 $\pm$1.1 $10^{17}$ cm$^{-2}$. The vector in the lower left of the figure shows the expected slope of the data for rotational temperatures of 300 K – van den Ancker et al. (1999) have shown that $H_2$ rotational temperatures lie in a narrow range from 200–500 K for a wide range of UV illumination in PDRs, and in $J$-shocks, but can range up to $\geq$ 1500 K in $C$-shocks. Most ground-based studies of the near-IR lines of $H_2$ have inferred rotational temperatures $\sim$ 2000–3000 K.

where $\nu$ are the wave-numbers (Dabrowski 1984) and $A\,(\nu'\,J')$ are the transition probabilities for the various transitions, taken from Turner et al. (1977). The column densities are then compared with those predicted for a thermal distribution characterised by a rotational temperature $T_{\rm rot}$ since the rotational populations of a given vibrational level can be approximated by a thermal distribution:

$$N(\nu'\,J')/g_j \propto \exp\left(-\frac{E(\nu'J')}{kT_{\rm rot}}\right) \quad (7)$$

In this relationship the $g$ terms are the degeneracies of the transitions, $g_j$ = (2$J$ + 1) for even $J$ (para-$H_2$) and $g_j$ = 3 $(2J+1)$ for odd $J$ (ortho-$H_2$), and the $E\,(\nu'\,J')$ terms represent the energy of the $(\nu'\,J')$ level. Thus the rotational temperature can be estimated from the inverse of the slope of a plot of $\ln\,(N\,(\nu'\,J')/g_j)$ against $E\,(\nu'\,J')/k$, correcting for an ortho/para ratio of 3:1.

It is clear from Fig. 23 that the $\nu$ = 0–0 lines are far less affected by extinction than the $\nu$ = 1–0 $S\,(1)$ lines. We can infer from the $2\,\sigma$ upper limits that the extinction to the $\nu$ = 1–0 $S\,(1)$ emitting gas must be $\lesssim 80^{\rm m}$ – otherwise we should have detected emission in the $\nu$ = 0–0 $S\,(6)$ or $S\,(7)$ lines, assuming that the rotational temperature is characteristic of many sources, $T_{\rm rot} \sim$ 2000 K. However, this limit is dominated by the S/N of the UKIRT spectra, and is not usefully stringent alone.

Shock models of the $H_2$ lines have been calculated by a number of workers. For $J$-shocks, 1D models have been presented by Brand et al. (1988), Hollenbach & McKee (1989), Burton et al. (1992), Neufeld & Hollenbach (1994), and for $C$-shocks, by Draine et al. (1983), Smith (1991), Kaufman & Neufeld (1996).

The ISOCAM CVF observations of Cabrit et al. (1999) made towards a number of molecular outflow sources show that the mid-IR $H_2$ lines dominate the cooling, and probe rotational temperatures in the range 300–2000 K. In the cases they studied, the observations were consistent with excitation in low-velocity $C$-shocks (10–30 km s$^{-1}$), based on the non-detection of $J$-shock tracers predicted to be present in the standard shock models of Hollenbach & McKee (1989), for shock velocities $\gtrsim$ 50 km s$^{-1}$. From the L1551 IRS 5 data set, we set $2\,\sigma$ upper limits of $2.5\times10^{-15}$ W m$^{-2}$ and $3.8\times10^{-15}$ W m$^{-2}$ on the Ni II $\lambda$ 6.64 and Ne II $\lambda$ 12.81 lines respectively.

To understand the excitation mechanism of the $H_2$, the $\nu$ = 2–1 $S\,(1)$ $\lambda$ 2.248 to $\nu$ = 1–0 $S\,(1)$ $\lambda$ 2.122 ratio has often been used as a diagnostic. This ratio has values typically $\sim$ 0.1 in shocked regions and molecular outflows, and $\sim$ 0.6 for pure fluorescence. However, Draine & Bertoldi (1996) show that in dense PDRs, thermal collisions can transfer the lower-level population ($\nu \leq 2$) towards LTE conditions, so that the line ratios approach those in shocked regions. Observational studies (Usuda et al. 1996; Takami et al. 1999) seem to confirm that this may indeed be the case. In one example, the case of the shocked region close to Orion KL, the ratio varies between $\sim$ 0.1 and 0.2 over a wide range of $\nu$ = 1–0 $S\,(1)$ intensity, whereas in a typical dense PDRs such as the Orion Bright Bar, and the reflection nebulae NGC 2023 and NGC 7023, the ratio varies between $\sim$ 0.2 and 0.6, and shows a clear anti-correlation with the $\nu$ = 1–0 $S\,(1)$ intensity. In L1551, the $2\,\sigma$ upper limit on the $\nu$ = 2–1 $S\,(1)$ $\lambda$ 2.248 line is $9.1\times10^{-19}$ W m$^{-2}$, and the $\nu$ = 2–1 $S\,(1)$ $\lambda$ 2.248 to $\nu$ = 1–0 $S\,(1)$ $\lambda$ 2.122 ratio is $\leq$ 0.11. Thus the ratio appears to be inconsistent with fluorescent excitation, even allowing for thermal collisions. This conclusion is consistent with the lack of an obvious ionising source in the centre of L1551. Although no firm conclusions can be reached on the basis of the line ratio data shown in Table 7, we can rule out (a) low density ($n_{\rm H_2} \sim 10^4$ cm$^{-3}$) shock models and (b) that the $H_2$ emission is seen through more than two or three magnitudes of visual extinction (because the $S\,(2)$ and $S\,(3)$ lines, which suffer from the highest extinction, would become too bright relative to any of the models). It thus seems most likely that the $\nu$ = 1–0 $H_2$ emission is seen in reflection.

### *4.6. CO vibrational bands*

The CO absorption against IRS 5 has been previously studied by Carr et al. (1987) although the new UKIRT data presented here have higher sensitivity and spectral resolution. The data shown in Fig. 24 are fitted by a gas temperature of 2500 K, Doppler width of 5 km s$^{-1}$, and CO gas phase column density of $6\times10^{20}$ cm$^{-2}$.

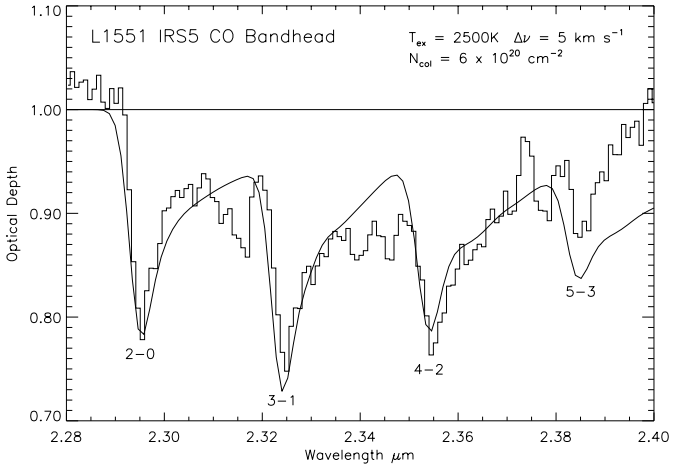


**Fig. 24.** CO gas modelling and ISO observations of IRS 5. For the upper pane, a model with $T_{\rm ex}$ = 2500 K and Doppler width $\nu_{\rm D}$ = 5 km s$^{-1}$ was run. The best fit column density = $6\times10^{20}$ cm$^{-2}$ is shown. Such high temperatures are needed to excite the CO bandhead, and to give the correct relative intensity ratios between the lines. The data and model have a resolution of 500.

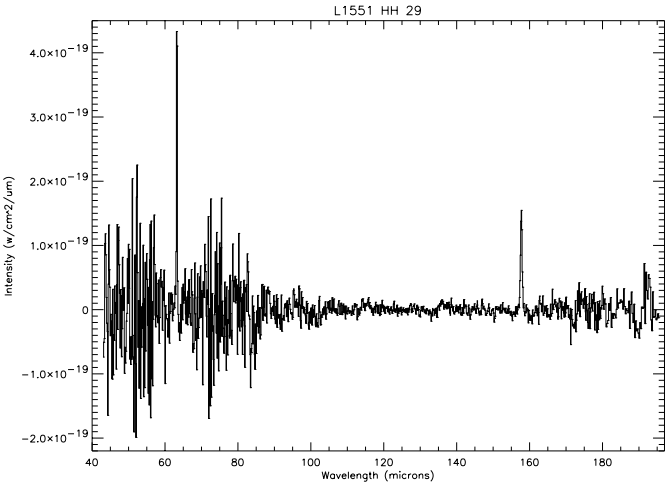


**Fig. 25.** HH 29 baseline subtracted spectrum.

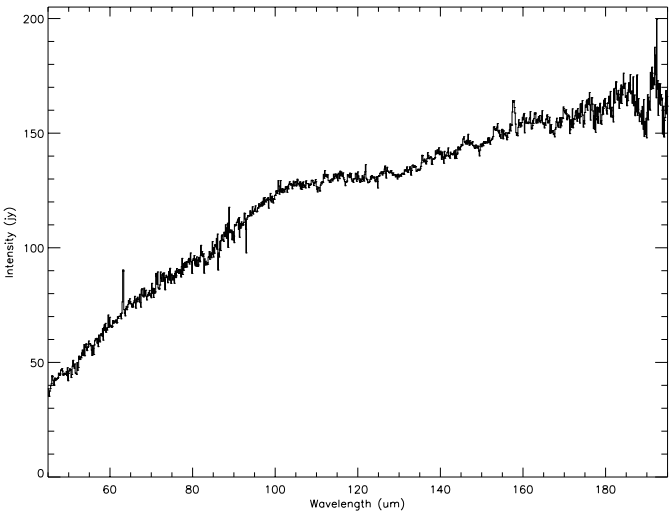


**Fig. 26.** LWS Spectrum of L1551 NE.

### *4.7. CO rotational lines*

It was not possible to detect rotational molecular CO line emission in any of the spectra. For the lowest-$J$ transitions towards L1551 IRS 5, we set $2\,\sigma$ upper limits for the $J$ =14–13 and $J$ =15–14 lines of $4.3\times10^{-17}$ W m$^{-2}$ and $1.37\times10^{-16}$ W m$^{-2}$ for L1551 IRS 5 and HH 29 respectively. L1551 appears unlike many other outflow sources, which are rich in shock excited CO line emission.

### *4.8. O I*

Towards L1551 IRS 5 the OI 63um flux is observed to be more intense than along the flow, which indicates that the emission is intrinsic and not due to the diffuse PDR. If the emission was due to the jet, then the mass loss rate is $\sim 7.6\times10^{-7}\ M_\odot$ yr$^{-1}$ (using the relationship from Hollenbach 1985), which is very similar to the $\sim 10^{-6}\ M_\odot$ yr$^{-1}$ derived from this source by other measurements. Along the flow it is likely that the OI emission comes from shocks in the outflows more than from diffuse PDR, since the OI lines are frequently brighter than the C I $\lambda$ 157 $\mu$m, particularly towards HH29, L1551 NE and on the b1,b2 and b3 positions, which are associated with peaks of C emission in the outflow map by Rainey et al. (1987) and Moriarty-Schieven & Snell (1988).

### *4.9. HH 29*

A deep (2 hour) observation with the LWS was also made centred on the location of HH 29. The baseline subtracted (fitting a low order polynomial to the continuum level) spectrum is shown in Fig. 24, and is devoid of line emission, except for the O I $\lambda$ 63.2 and C II $\lambda$ 157.7 lines as listed in Table 1.

### *4.10. L1551 NE*

A red 6 $L_\odot$ source has been reported lying close to IRS 5, which has become known as L1551 NE (Emerson et al. 1984). This source has been imaged by Draper et al. (1985) and Campbell et al. (1988). Moriarty-Schieven et al. (1995) first suggested that L1551 NE was the source of a second outflow close to IRS 5, and subsequent observations by Devine et al. (1999) indicated that L1551 NE may be responsible for driving the Herbig-Haro flow HH454. Observations of the continuum towards L1551 NE were also made, and are shown in Fig. 26. This spectrum shows little evidence of any line emission, other than reported in Table 1.

### *4.11. Other locations along the outflow*

Observations at a number of other locations along the molecular outflow, revealed no emission apart from weak C II and O I lines, and will not be further discussed here.

## 5. Conclusions

Observations have been made towards the two well known infrared sources L1551 IRS 5 and L1551 NE, and at a number of locations in the molecular outflow, using the LWS and SWS spectrometers on the ISO satellite, and several other near-IR telescopes. The present work possibly adds to the complexity by unveiling a plethora of unexpected phenomena, such as e.g. the occurence of significant extinction at mid and far infrared wavelengths and the existence of dense and hot regions (thermally stable?) over extended scales. The main results of this study are:

1. The ISO LWS spectrum consists of a relatively strong continuum, superposed with a few weak lines of O I, C II and possibly OH. Emission from other species such as CO or $H_2O$ was not detected. This might indicate that either the molecules have been destroyed, perhaps in a shock, or that the environment is unable to excite them to emit in the far and near infrared.
2. The ISO SWS spectrum of L1551 IRS 5 contains solid state absorption lines of CO, $CO_2$, $H_2O$, $CH_4$ and $CH_3OH$, which correspond to column densities of $\geq 7.7\times10^{18}$ cm$^{-2}$, $5.4\times10^{17}$ cm$^{-2}$, $7.6\times10^{16}$ cm$^{-2}$ and $2.6\times10^{18}$ cm$^{-2}$ respectively.
3. Examination of archival HST NICMOS images reveals a diffuse conical shaped nebulosity, due to scattered light from the central object, with a jet emanating from L1551 IRS 5. It is likely that the emission in this jet-like feature is dominated by [Fe II] lines.
4. The continuum spectral energy distribution has been modelled using a 2D radiative transfer model. The continuum is well fitted for a central source luminosity of 45 $L_\odot$, surrounded by a flared disc with an opening angle of 90°. The outer parts of the torus extend to a distance of $\sim 3\times10^4$ AU, and has a total (gas + dust) mass of $\sim 13\,M_\odot$. The extinction towards the outflow is estimated to be $A_{\rm v} \approx 10$ and the mid-plane optical depth to L1551 IRS 5 to be $\approx 120$. This model provides a good fit to the ISO data, as well as the available HST/NICMOS data, mid-IR maps, submm interferometry, and ground-based photometry with a range of different aperture sizes.
5. On the basis of the above model, an extinction curve has been estimated, which shows that the emission at wavelengths shorter than $\sim 2\,\mu$m is due to scattered light from close to L1551 IRS 5, while at wavelengths $\gtrsim 4\,\mu$m, is seen through the full extinguishing column towards the central source. This need to be taken careful account of when comparing line intensities at different wavelengths.
6. Three [Fe II] lines were detected in the SWS spectrum towards L1551 IRS 5, with a fourth line at $\sim 1.5\,\sigma$, and upper limits on several others. Although it would seem at first sight that shocks would be the most likely source of excitation in a known shocked region such as this, the line intensities do not fit the predictions of simple shock models. The problem with such shock interpretation of the [Fe II] lines is that the line ratios and strengths imply densities and temperatures which are outside the range considered by Hollenbach & McKee. However, as explained in 4.1.1 4.1.3, the overall energy budget and observed densities place stringent limits on possible shock models, leading us to explore other models. An alternative explanation has been examined where the [Fe II] gas is hot ($\sim 4000$ K) and dense ($n_{\rm H_2} \gtrsim 10^9$ cm$^{-3}$). Although this provides an acceptable fit to the relative line intensities, it provides no constraints as to the precise heating mechanism of the gas – although it seems likely that it would have to occur very close to the root of the outflow. The lack of detection on Br $\alpha$ $\lambda$ 4.052 or Br $\gamma$ $\lambda$ 2.626, and the known low surface temperature ($T_{\rm eff} \sim 5500$ K) of the central protostellar object argue against efficient excitation in a high UV field environment, making shocks the most likely way to explain the [Fe II] and [Si II] emission intensities.
7. The SWS observations did not detect any emission from rotationally excited $H_2$. Observations with UKIRT of the vibrationally excited $S$ and $Q$-branch lines were consistent with the gas having an excitation temperature of $\sim 2500$ K. Given the likely opacity to the central source which was predicted in our modelling, it is unlikely that we would have detected emission due to this hot gas component. Similarly, there was no evidence of lower temperature ($\sim 500$ K) gas, as has been inferred towards many other sources.
8. Observations with UKIRT of the CO absorption bands close to 2.4 $\mu$m are best fit with gas temperatures $\sim 2500$ K, and a column density $\sim 6\times10^{20}$ cm$^{-2}$.
9. Evidence for dense (coronal and higher densities) and hot (at least 2500 K up to perhaps 5000 K) gas is manifest in a multitude of observables; a) the overall SED, b) the CO bands, c) for a 'normal' [CO]/[$H_2$] = 8 $10^{-5}$, the implied $H_2$ colum density N($H_2$) = 6 $10^{20}$/8 $10^{-5}$ = 8 $10^{24}$ $\sim 10^{25}$ cm$^{-2}$ for gas at T $\gtrsim$ 2500 K, d) the $H_2$ emission (presence of rovibrational emission and absence of pure rotational lines) e) the [Fe II] spectrum, and f) that the SiII 35 micron is also consistent with this gas.
   Although each of these individual pieces of evidence may have several interpretations, we argue that the combination of them all makes it highly likely that such a hot and dense gas phase is present. The problem as how to produce and to maintain this region (which has not previously been presented in the literature elsewhere) is beyond the scope of the present paper. Our simple modelling is based on steady state assumptions about processes which are most probably highly dynamic in nature. Any attempt to provide an explanation(s) would at the moment be based on pure speculation, and so we instead indicate the need for extensive theoretical work, which is beyond the scope of the present observational paper.
10. Observations at a number of other locations along the molecular outflow, and towards the Herbig-Haro object HH29, revealed no emission apart from weak C II and O I lines.

*Acknowledgements.* The Second Palomar Sky Survey (POSS II) was made by the California Institute of Technology with funds from the National Science Foundation, The National Geographic Society, The Sloan Foundation, The Samuel Oschin Foundation, and the Eastman

Kodak Corporation. We thank Dr Malcolm Fridlund for discussions about his unpublished echelle spectra towards the L1551 IRS 5 outflow jet, Dr Janet Bowey for comments about the mineralogy of dusty circumstellar environments, Dr Frossie Economou for helping us recover the UKIRT archive data, and the referee Dr Michiel Hogerheijde for some helpful comments.

## References

Asplund M., 2000, A&A 359, 755
Bergin E.A., Melnick G.J., Neufeld D.A., 1998, ApJ 499, 774
Bergin E.A., Melnick G.J., Neufeld D.A., 1999, ApJ 510, L145
Bieging J.H., Cohen M., 1985, ApJ 289, L5
Black J., van Dishoeck E.F., 1987, ApJS 322, 412
Boogert A., Schutte W.A., Tielens A.G.G.M., et al., 1996, A&A 315, L377
Brand P.W.J.L., Moorhouse A., Burton M.G., et al., 1988, ApJ 334, L103
Burton M.G., Hollenbach D.J., Tielens A.G.G.M., 1992, ApJ 399, 563
Butner H.M., Evans II N.J., Lester D.F., et al., 1991, ApJ 376, 636
Butner H.M., Natta A., Evans N.J., 1994, ApJ 420, 326
Cabrit S., Bontemps S., Lagage P.O., et al., 1999, Proc ESA Conference on ISO, Paris, 1998
Campbell B., Persson S.E., Strom S.E., et al., 1988, AJ 95, 1185
Callaway J., 1994, Atomic Data and Nuclear Tables 57, 9
Carr J.S., Harvey P.M., Lester D.F., 1987, ApJ 321, L71
Ceccarelli C., Caux E., Loinard L., et al., 1999, A&A 342, L21
Chiar J.E., Tielens A.G.G.M., Whittet D.C.B., et al., 2000, ApJ 537, 749
Clegg P.E., Ade P.A., Armand. C., et al., 1996, A&A 315, L38
Cohen M., Fuller G.A., 1985, ApJ 296, 620
Dabrowski I., 1984, Canadian J. Phys. 62, 1639
Dartois E., Schtte W., Geballe T.R., et al., 1999, A&A 342, 32
de Graauw Th., Haser L.N., Beintema D.A., et al., 1996, A&A 315, L49
Devine D., Reipurth B., Bally J., 1999, AJ in press
Draine B.T., Bertoldi F., 1996, ApJ 468, 269
Draine B.T., Roberge W.G., Dalgarno A., 1983, ApJ 264, 485
Draper P.W., Warren-Smith R.F., Scarrott S.M., 1985, MNRAS 216, 7P
Emerson J.P., Harris S., Jennings R.E., et al., 1984, ApJ 278, L49
Ferland G.J., Korista K.T., Verner D.A., et al., 1998, PASP 110, 761
Fridlund C.V.M., Liseau R., 1988, ApJ 499, L75
Fridlund M., White G.J., 1989a, In: Winnewisser G. (ed.) Physics and Chemistry of Molecular Clouds. p. 198
Fridlund M., White G.J., 1989b, A&A 223, L13
Fridlund C.V.M., Huldtgren M., Liseau R., 1997, IAU 182, p. 19
Fridlund C.V.M., Liseau R., Perryman M., 1993, A&A 273, 601
Gerakines P.A., Schutte W.A., Greenberg J.M., van Dishoeck E.F., 1995, A&A 296, 810
Giovanardi C., Rodríguez L.F., Lizano S., Cantó J., 2000, ApJ 538, 728
Greenhouse M.A., Satyapal S., Woodward C.E., et al., 1997, ApJ 476, 105
Grevesse N., Sauval A.J., 1999, A&A 347, 348
Haas M.R., Hollenbach D.J., Erickson E.F., 1986, ApJ 301, L57
Hollenbach D.J., 1985, Icarus 61, 40
Hollenbach D.J., McKee C.F., 1989, ApJ 342, 306
Hollenbach D.J., Chernoff D.F., McKee C.F., 1989, ESA SP-290, 245
Hollenbach D.J., Takahashi T., Tielens A.G.G.M., 1991, ApJ 377, 192
Itoh Y., Kaifu N., Hayashi M., et al., 2000, PASJ 52, 81
Justtanont K., Tielens A.G.G.M., de Jong T., et al., 1999, A&A 345, 605
Kaufman M.J., Neufeld D.A., 1996, ApJ 456, 611
Kaufman V., Sugar J., 1986, J. Phys. Chem. Ref. Data 15(1), 321
Keane J.V., Tielens A.G.G.M., Boogert A.C.A., et al., 1999, The Universe as seen by ISO. ESA SP-427, 683
Keene J., Masson C.R., 1990, ApJ 355, 635
Lay O.P., Carlstrom J.E., Hills R.E., et al., 1994, ApJ 434, L75
Liseau R., Ceccarelli C., Larsson B., et al., 1996, A&A 315, L181
Looney L.W., Mundy L.G., Welch W.J., 1997, ApJ 484, L157
Lucas P.W., Roche P.F., 1996, MNRAS 280, 1219
Lutz D., Feuchtgreuber H., Genzel R., et al., 1996, A&A 315, 269
Lutz D., Genzel R., Kunze D., et al., 1998, Star Formation with the Infrared Space Observatory. ASP Conf. Ser. vol. 132, p. 89
Men'shchikov A.B., Henning Th., 1997, A&A 318, 879 (MH97)
Men'shchikov A.B., Henning Th., Fischer O., 1999, ApJ 519, 257 (MHF99)
Melnick G.J., Genzel R., Lugten J.B., 1987, ApJ 321, 530
Moorwood A.F.M., Oliva, 1988, A&A 203, 278
Moriarty-Schieven G.H., Snell R.L., 1988, ApJ 332, 364
Moriarty-Schieven G.H., Butner H.M., Wannier P.G., 1995, ApJ 445, L55
Mundt R., Fried J.W., 1983, ApJ 274, L83
Neufeld D.A., Hollenbach D.J., 1994, ApJ 428, 170
Neufeld D.A., Chan W., Melnick G.J., et al., 1996, A&A 315, L237
Nisini B., Benedettini M., Giannini T., et al., 1999, A&A 350, 529
Oliva E., Moorwood A.F.M., Drapatz S., Lutz D., Sturm E., 1999a, A&A 343, 943
Oliva E., Lutz D., Drapatz S., Moorwood A.F.M., 1999b, A&A in press
Pendelton Y.J., Tielens A.G.G.M., Tokunaga A.T., Bernstein M.P., 1999, ApJ 513, 294
Quinet P., Le Dourneuf M., Zeippen C.J., 1996, A&AS 120, 361
Rainey R., White G.J., Richardson K.J., et al., 1987, A&A 170, 237
Rodríguez L., Cantó J., Torrelles J.M., et al., 1986, ApJ 301, L25
Rodríguez L., D'Alessio P., Wilner D.J., et al., 1999, Nat 395, 355
Saraceno P., Nisini B., Benedettini M., et al., 1999, In: Cox P., Kessler M. (eds.) The Universe as seen by ISO. ESA SP-427.p. 575
Smith H., Fischer J., Geballe T.R., et al., 1987, ApJ 316, 265
Smith M.D., 1991, MNRAS 253, 175
Snell R.L., Loren R.B., Plambeck R.L., 1980, ApJ 239, L17
Stocke J.T., Hartigan P., Strom S.E., et al., 1988, ApJS 68, 229
Swinyard B., Clegg P.E., Ade P.A.R., et al., 1996, A&A 315, L43
Takami M., Usuda T., Sugai H., et al., 1999, ApJ 529, 268
Tielens A.G.G.M., Allamandola L.J., Bregman J., et al., 1984, ApJ 287, 697
Tegler S.C., Weintraub D.A., Allamandola L., et al., 1993, ApJ 411, 260
Turner J., Kirby-Docken K., Dalgarno A., 1977, ApJS 35, 281
Usuda T., Sugai H., Kawabata H., et al., 1996, ApJ 464, 818
Woody D.P., Scott S.L., Scoville N.Z., et al., 1989, ApJ 337, L41
van den Ancker M.E., Bouwman J., Wesselius P.R., et al., 1999, A&A 357, 325
Walker C.K., Adams F.C., Lada C.J., 1990, ApJ 349, 515
Wesselius P.R., van den Ancker M.E., Tielens A.G.G.M., et al., 1998, Star Formation with the Infrared Space Observatory 132, 287
Wiese W.L., Smith M.W., Glennon B.M., 1966, Atomic Transition Probabilities. NSRDS-NBS 4, US National Bureau of Standards
White G., Parker N., Hayashi S., et al., 1991, A&A 250, 134
Zhang H.L., Pradhan A.K., 1995, A&A 293, 953